

# Proper Motions of Dwarf Spheroidal Galaxies from *Hubble Space Telescope* Imaging. I: Method and a Preliminary Measurement for Fornax.<sup>1</sup>

Slawomir Piatek

Dept. of Physics, New Jersey Institute of Technology, Newark, NJ 07102

E-mail address: piatek@physics.rutgers.edu

Carlton Pryor

Dept. of Physics and Astronomy, Rutgers, the State University of New Jersey,  
136 Frelinghuysen Rd., Piscataway, NJ 08854-8019

E-mail address: pryor@physics.rutgers.edu

Edward W. Olszewski

Steward Observatory, University of Arizona, Tucson, AZ 85721

E-mail address: eolszewski@as.arizona.edu

Hugh C. Harris

US Naval Observatory, Flagstaff Station, P. O. Box 1149, Flagstaff, AZ 86002-1149

E-mail address: hch@nofs.navy.mil

Mario Mateo

Dept. of Astronomy, University of Michigan, 830 Dennison Building, Ann Arbor, MI  
48109-1090

E-mail address: mateo@astro.lsa.umich.edu

Dante Minniti

Department of Astronomy, Pontificia Universidad Católica, Av. Vicuña Mackenna 4860,  
Santiago 22, Chile

E-mail address: dante@astro.puc.cl

David G. Monet

US Naval Observatory, Flagstaff Station, P. O. Box 1149, Flagstaff, AZ 86002-1149

E-mail: dgm@nofs.navy.mil

Heather Morrison

---

<sup>1</sup>Based on observations with NASA/ESA *Hubble Space Telescope*, obtained at the Space Telescope Science Institute, which is operated by the Association of Universities for Research in Astronomy, Inc., under NASA contract NAS 5-26555.

Department of Astronomy and Department of Physics, Case Western Reserve University,  
10900 Euclid Avenue, Cleveland, OH 44106-7215  
E-mail address: heather@vegemite.astr.cwru.edu

Christopher G. Tinney  
Anglo-Australian Observatory, PO Box 296, Epping, 1710, Australia  
E-mail address: cgt@aaoepp.aao.gov.au

## ABSTRACT

This article presents and discusses a method for measuring the proper motions of the Galactic dwarf spheroidal galaxies using images taken with the Hubble Space Telescope. The method involves fitting an effective point spread function to the image of a star or quasi-stellar object to determine its centroid with an accuracy of about 0.005 pixel (0.25 milliarcseconds) — an accuracy sufficient to measure the proper motion of a dwarf spheroidal galaxy using images separated by just a few years. The data consist of images, dithered to reduce the effects of undersampling, taken at multiple epochs with the Space Telescope Imaging Spectrograph or the Wide Field Planetary Camera. The science fields are in the directions of the Carina, Fornax, Sculptor, and Ursa Minor dwarf spheroidal galaxies and each has at least one quasi-stellar object whose identity has been established by other studies. The rate of change with time of the centroids of the stars of the dwarf spheroidal with respect to the centroid of the quasi-stellar object is the proper motion.

Four independent preliminary measurements of the proper motion of Fornax for three fields agree within their uncertainties. The weighted average of these measurements is  $\mu_\alpha = 49 \pm 13$  milliarcseconds century<sup>-1</sup> and  $\mu_\delta = -59 \pm 13$  milliarcseconds century<sup>-1</sup>. The Galactocentric velocity derived from the proper motion implies that Fornax is near perigalacticon, may not be bound to the Milky Way, and is not a member of any of the proposed streams of galaxies and globular clusters in the Galactic halo. If Fornax is bound, the Milky Way must have a mass of at least  $(1.6 \pm 0.8) \times 10^{12} \mathcal{M}_\odot$ .

*Subject headings:* galaxies: dwarf spheroidal — galaxies: individual (Fornax) — astrometry: proper motion

## 1. Introduction

There are nine known dwarf spheroidal (dSph, hereafter) galaxies in relative proximity to the Milky Way, (see Mateo 1998 and van den Bergh 2000 for reviews). The nearest, Sagittarius, is only about 16 kpc from the Galactic center and it is moving on a polar orbit. The most distant dSph, Leo I, is 250 kpc from the Galactic center. The average distance from the Sun of the whole population of dSphs is roughly 100 kpc. Although these distances are small compared to the size of the Local Group, they are sufficiently large to have made proper motion measurements very difficult using images obtained with ground-based telescopes. The effect of large distance on the size of the proper motion can be lessened by a long interval between image epochs — the time baseline. However, many of the nine dSphs were discovered only in the past several decades (the most recent, Sagittarius, in 1994) and, thus, the available images of dSphs with a quality high enough for proper motion measurements have insufficient time baselines.

Despite these difficulties, several groups have reported proper motions for a few dSphs. Scholtz & Irwin (1993) used Schmidt plates with a time baseline of about 35 years to measure a proper motion,  $(\mu_\alpha, \mu_\delta)^2$ , for Draco of  $(90 \pm 50, 100 \pm 50)$  milliarcseconds per century ( $\text{mas cent}^{-1}$ , hereafter) and a proper motion for Ursa Minor of  $(100 \pm 80, 100 \pm 80) \text{ mas cent}^{-1}$ . Schweitzer et al.(1995) used a variety of larger-scale plates with a time baseline of about 50 years to measure a proper motion for Sculptor of  $(36 \pm 22, 43 \pm 25) \text{ mas cent}^{-1}$ . Similarly, Schweitzer et al.(1997) used Palomar 5 m and KPNO 4 m plates with a time baseline of 42 years to measure a proper motion for Ursa Minor of  $(58 \pm 8, 26 \pm 10) \text{ mas cent}^{-1}$ . Finally, Irwin et al. (1996) used Schmidt plates to measure a preliminary proper motion for Sagittarius of  $210 \pm 70 \text{ mas cent}^{-1}$ . All of the above proper motions are corrected for the motion of the Local Standard of Rest (LSR, hereafter) and the peculiar motion of the Sun with respect to the LSR. The small number and, in most cases, the large uncertainties of the existing measurements emphasizes the difficulties inherent in measuring the proper motion of a dSph. Accurate proper motions of dSphs would explain or help to answer a number of outstanding questions about the dSphs themselves, the Milky Way, interactions between dSphs and the Milky Way, and the formation of galaxies. Probably the most fundamental question is whether a dSph is gravitationally bound to the Milky Way. Satellite status is almost universally assumed for the known dSphs — confirming this assumption requires, among other things, a knowledge of the proper motion of each dSph.

---

<sup>2</sup>Throughout this article,  $\mu_\alpha$  is the proper motion in arcseconds in the direction of increasing right ascension, *i.e.*, the actual shift on the sky in that direction. The same is true for  $\mu_\ell$ , the proper motion in the direction of increasing galactic longitude.

Using the Hubble Space Telescope (HST, hereafter) for astrometry has advantages over using a ground-based telescope. HST has superior angular resolution which, in principle, allows a more precise measurement of the location of an object. This in turn reduces the required time baseline between images of a dSph to just a few years. As an example, consider an “average” dSph at a heliocentric distance of 100 kpc with an assumed tangential velocity with respect to the Sun of  $220 \text{ km s}^{-1}$ . Then the expected heliocentric proper motion of the dSph is  $46 \text{ mas cent}^{-1}$ . Assuming a plate scale of  $51 \text{ mas pixel}^{-1}$  for the CCD imager in HST cameras, the expected shift in the position of the dSph over a one-year period is about 0.009 pixel.

Several ground-based astrometric programs (Monet et al. 1992; Tinney et al. 1995; Tinney 1996) have shown that shifts of this magnitude can be measured with CCD detectors. CCD detectors used in differential, small-angle astrometric measurements have significantly smaller systematic errors compared to measurements with a long time baseline using photographic plates, which are almost always acquired on different telescopes and which have increased uncertainties because of digitization on scanning machines.

A single HST image of a stellar field is undersampled because the full width at half of maximum (FWHM, hereafter) of a stellar point-spread function (PSF, hereafter) is only about 1.0 pixel for the HST imaging detectors. Undersampling causes an image to have a “digitized” appearance and it makes measuring the centroid of a star to an accuracy of few thousandths of a pixel impossible with just a single image of the star. Lauer (1999) and Anderson & King (2000) discuss these and other problems associated with undersampling and offer remedies for these shortcomings. They show that accurate centroids of undersampled stellar images can be measured from multiple images of a science field which are dithered in a pattern which, for example, is an  $N \times N$  grid of  $1/N$  subpixel steps (Lauer 1999), where  $N^2$  is the number of images. Such dithered images allow the construction of a well-sampled effective point-spread function (ePSF, hereafter), which is the convolution of the PSF of the telescope and the function representing the spatial response of a pixel in the CCD detector. The value of the ePSF at a specific distance and direction from its center is the response (formally the fluence: photon counts per readout, though this article uses the more colloquial term flux) measured by a pixel at that distance from the centroid of the star. The centroid of an object and its brightness can be determined by fitting the ePSF to the measured flux in an array of pixels corresponding to the object. Even though the individual functions in the convolution defining the ePSF can be difficult, or even impossible, to ascertain, the ePSF can be constructed without knowing an explicit form for these functions. Anderson & King (2000) describe in detail a method for constructing the ePSF and a procedure for fitting the ePSF to the data in order to determine the centroid and total flux of an object. Bernstein (2002) provides additional discussion of these topics. Our method of constructing the ePSF,

discussed in this article, is very similar to that described in Anderson & King (2000).

The expected small size of the proper motion of a dSph requires that the reference frame be defined by extragalactic objects. The images of quasi-stellar objects (QSOs) are more compact at a given brightness than are the cores of ordinary galaxies, making a QSO a better reference frame than such a core. For this reason (and because bright QSOs are useful probes for gas in dSphs), Cudworth, Olszewski, & Schommer (1986), Tinney, Da Costa, & Zinnecker (1997), and Tinney (1999) (and references therein) undertook searches for QSOs behind the dSphs. Of the resulting QSOs, those that provide the required inertial reference frame with the minimum exposure time have magnitudes comparable to those of the brightest stars of the dSph that are in a typical HST field.

We are carrying out a program to measure proper motions for four dSphs — Carina, Fornax, Sculptor, and Ursa Minor — from HST images taken at three epochs, each separated by 1 – 2 years. This article serves the following purposes. 1) It describes our method for deriving an ePSF and for fitting it to the data to find the centroids of objects. 2) It examines how accurately proper motions of the dSphs can be measured using our methods and data. 3) Finally, the article presents a preliminary proper motion of Fornax derived from two- or three-epoch data for three distinct fields and discusses its implications.

## 2. Data

The data consist of images of fields in the Carina, Fornax, Sculptor, and Ursa Minor dSphs obtained using HST with either the Planetary Camera (PC; the high-resolution camera of the Wide Field and Planetary Camera 2 – WFPC2) with the F606W filter or the Space Telescope Imaging Spectrograph (STIS) with no filter (50CCD). Columns 1 and 2 in Table 1 give the name of each field and the detector with which it was imaged. The third column gives the dates of the observations, both existing and planned. The fourth column gives the number of exposures in the field and the average exposure time for each. The remaining columns give the right ascension, declination, galactic longitude, and galactic latitude of the center of each field, respectively. The fields are approximately centered on known QSOs located in the directions of the dSphs (Cudworth, Olszewski, & Schommer 1986; Tinney, Da Costa & Zinnecker 1997; Tinney 1999). The QSO in the FOR 0240 – 3434 field is a gravitational lens with two images (Tinney 1995). We currently have three epochs of data for four fields and two epochs of data for all but one of the remaining fields, where consecutive epochs are about one or two years apart (see column 3 of Table 1). At each epoch, there are observations at eight dither positions. The target dither pattern consists of two quartets of pointings, where each quartet forms a square with a side of 0.5 pixel. The two quartets

are shifted with respect to each other by 0.25 pixel in both the  $X$  and  $Y$  directions. This pattern forms a square grid with a spacing of  $\sqrt{2}(0.25)$  pixel rotated by an angle of 45 degrees with respect to the  $X$  axis. For the STIS data, an error in setting up the dither distorted the target pattern so that alternate lines of the square grid are shifted along the line by  $\sqrt{2}(0.125)$  pixel. The error appears to have had no effect on our ability to measure proper motions. The target pattern also includes integer pixel offsets to shift the position of objects with respect to hot pixels. The STIS data has three images (cosmic ray splits) per dither position, while for the PC data the number of images per dither position varies between one and five. The exposure time of the individual images is the longest possible time that does not saturate the image of the QSO and that satisfies the scheduling constraints imposed by the window of visibility during the HST orbit.

The PC detector is a  $800 \times 800$  pixel CCD chip with a plate scale of about  $0.046 \text{ arcsec pixel}^{-1}$ . Because of vignetting by the pyramidal mirror, the usable area of a PC image is  $34.4 \text{ arcsec} \times 33.7 \text{ arcsec}$ . The STIS detector is a single  $1024 \times 1024$  pixel CCD chip with a plate scale of about  $0.051 \text{ arcsec pixel}^{-1}$ . Because of vignetting near the edges of the detector, the usable area is only approximately the central  $50 \times 50 \text{ arcsec}^2$ . The gain for all of the PC data is 7 electrons per digital unit and for all of the STIS data it is 1 electron per digital unit.

The standard HST pipeline corrected the STIS and PC images for the electronic bias, the dark current from hot pixels, and non-uniform sensitivity (the flat-field). In the case of the STIS images, the pipeline also removes cosmic rays by combining the three images taken at each dither position. As part of this last correction, the pipeline produces a record of the pixels affected by cosmic rays for both the individual and the combined images. The STIS pipeline produces three arrays for each image (and each combined image): 1) the corrected pixel photon counts, which we refer to as the science image or the science data depending on the context; 2) the uncertainties in the pixel photon counts; and 3) a word of 16 flags indicating (if non-zero) some problem associated with the pixel (see Brown et al. 2002 for the definitions of the flags). The PC pipeline produces two arrays for each image: the pixel photon counts and an array of flags (see Baggett et al. 2002). The uncertainty of each pixel value for the PC images is calculated from the value, gain, read noise, and a 0.3% flat-field noise.

### 3. Measurement of the Proper Motion

The task of measuring the proper motion of a dSph consists of four broad steps: 1) identifying objects, 2) constructing the ePSF, 3) determining centroids of objects by fitting

the ePSF, and 4) calculating the proper motion from the sets of centroids at different epochs. Steps 2) and 3) are inter-dependent because the construction of the ePSF requires accurate centroids. The remainder of this section presents a brief introduction to these steps while a more detailed discussion follows in the rest of the article.

Using the DAOPHOT package, we find the QSO and stars in the field and determine their approximate location and brightness. Our fields contain relatively few stars, 100 – 600, and most of them are faint. This number of stars is a small fraction of those available in similar published astrometric studies using HST (King et al. 1998; Bedin et al. 2001; Kuijken & Rich 2002). The small number of stars in our fields has an adverse impact on steps 2), 3), and 4). For example, the small number of stars limits both the accuracy of the ePSF and the knowledge of changes in the ePSF with position within a field. To ameliorate the impact of the small number of stars on the accuracy of the ePSF, we use all of the dither images available for a field at a given epoch to generate a single ePSF. This procedure effectively increases the number of stars contributing to the ePSF, at the cost of assuming that the ePSF neither varies among the images at one epoch or within the images.

If the image of the QSO is more extended than that of a star, then including the QSO in the construction of the ePSF may distort the ePSF. Fitting such an ePSF could lead to systematic errors in the centroids of both the stars and the QSO. These systematic errors will affect the measured proper motion if they are different at different epochs. The errors could differ among epochs if, for example, the shapes of stellar images change because of guiding jitter. The  $\chi^2$  resulting from fitting the ePSF to the QSO is similar to those resulting from fitting to bright stars. Thus, our procedure is to include the QSO in the construction of the ePSF to improve the signal-to-noise ratio ( $S/N$ ) of the ePSF.

A quartic kernel provides the weight with which an observed pixel value contributes to each point of the grid which defines the ePSF and the average of these values is the initial estimate of the ePSF. Iteratively applying the same interpolation and averaging scheme to the difference between the observed pixel values and the ePSF refines the estimate of the ePSF. Forcing weighted moments of the ePSF to be zero maintains a consistent centering of the ePSF on its grid among epochs. The centroids of objects come from fitting the ePSF to observed pixel values using least squares. The estimation and fitting procedures are similar for the PC and STIS images, with differences arising primarily from the availability of combined images with cosmic ray rejection for the STIS data.

The output of constructing and fitting the ePSF is a centroid for each star in the field,  $(X_{0,i}(t), Y_{0,i}(t))$  – here  $i$  is the index of a star, and for the QSO,  $(X_{0,Q}(t), Y_{0,Q}(t))$  at at least two epochs:  $t_1, t_2, \dots$ . Also output is the uncertainty in these centroids, which are calculated from the scatter of the individual values derived from each image at a given epoch around

their mean.

The proper motion of the dSph causes a change in the average position of its stars with respect to the QSO. The measured centroids differ among epochs both because of the proper motion and because of differences in pointing, image rotation, and image scale. Measuring the proper motion requires a consistent coordinate system among all epochs. But the centroid of the QSO at two epochs only contains enough information to determine the difference in pointing. Thus, we use the stars of the dSph to define a standard coordinate system and determine the four-parameter transformation ( $X$  and  $Y$  offsets, rotation, and relative scale) that relates the coordinate systems at different epochs. The measured proper motion of the dSph is then the opposite of the change in the centroid of the QSO in the standard coordinate system.

Geometrical distortions introduced by the STIS and WFPC2 optics could require a more complex transformation between the coordinate systems at pairs of epochs. A more complex transformation has more degrees of freedom and, therefore, requires more stars to determine it accurately. Given the small number of stars in a typical field, introducing more than four parameters into the transformation could degrade significantly the accuracy of the measured proper motion. We minimize the need for a more complex transformation by both removing the best estimates of the distortions and, more importantly, by putting objects back on the same pixel of the detector as closely as possible at the different epochs. The latter ensures that any uncorrected distortion is the same at both epochs and, so, does not affect the measured proper motion.

The two components of the change in the centroid of an object in the standard coordinate system between two epochs are

$$p_x = X_0^{tr}(t_2) - X_0(t_1) \quad (1)$$

$$p_y = Y_0^{tr}(t_2) - Y_0(t_1). \quad (2)$$

In the above equations,  $(X_0^{tr}(t_2), Y_0^{tr}(t_2))$  are the coordinates of an object at the second epoch transformed into the standard coordinate system of the first epoch,  $t_1$ . The uncertainties in  $p_x$  and  $p_y$  have contributions from the uncertainties of the measured centroids at the two epochs and from the uncertainty in the transformation. The proper motion of the dSph is proportional to  $-p_x$  and  $-p_y$  of the QSO.



## 4. Selecting Objects

### 4.1. Initial Estimate of Centroids for Objects

The initial estimate of the centroids of objects and of their magnitudes comes from processing the images with the DAOPHOT and ALLSTAR software packages (Stetson 1987, 1992, 1994). The DAOPHOT task FIND distinguishes objects in the images. The objects are stars (stars of the dSph and foreground stars of our Galaxy), galaxies, QSOs, and, unwontedly, spurious objects such as cosmic rays and “hot pixels.” A visual examination of the images eliminates galaxies and close pairs of stars from further consideration. Photometry based on PSF fitting by ALLSTAR gives the locations and magnitudes of objects. Subsequently, DAOMATCH and DAOMASTER match the objects found in individual images and derive translations between the locations in different images. The master list of all objects found in the images and the set of translations provide the first estimate of the centroids of objects.

### 4.2. Extracting Objects from Images

Because of the undersampling in the PC and STIS CCDs, all of the information about the brightness and location of an object is contained in only a few pixels. For convenience, we extract from the science image a  $5 \times 5$  array of pixel values centered on the DAOPHOT centroid of an object as shown in Figure 1. Here  $p$  and  $q$  are the indices of the pixel that contains the centroid of the object,  $(X_0, Y_0)$ . In the figure, a plus marks the center of each pixel and the slanted cross marks the centroid of the object. The relationships between  $(X_0, Y_0)$  and  $(p, q)$  are

$$p = \text{Int}(X_0) + 1 \tag{3}$$

$$q = \text{Int}(Y_0) + 1. \tag{4}$$

In these equations, the function *Int* takes the integer part of its argument. Our convention for indexing pixels and for the coordinates of the center of a pixel determine Equations 3 and 4: the pixel in the lower left corner of an image has indices (1, 1) and its center has coordinates (0.5, 0.5). Note that this convention for the coordinates of the center of a pixel differs from that used in DAOPHOT, where the center of the lower left pixel has coordinates (1.0, 1.0). Our computer code takes this difference into account when it reads the master list.

For each object we also extract from the FITS files the corresponding  $5 \times 5$  array containing data-quality flags and, for STIS, the corresponding  $5 \times 5$  array containing the

uncertainties of the pixel values.

### 4.3. Sky Subtraction

The signal in the  $5 \times 5$  science data array comes from the central object and from “the sky” — scattered light and light from unresolved galaxies and stars. Our images are empty enough that an accurate estimate of the sky is the median value of those pixels whose centers are in an annulus centered on the object with inner and outer radii of 8.0 and 16.0 pixels, respectively. The sky is subtracted from the signal of each pixel in the science data array to ensure that only light from the central object contributes to the construction and fitting of the ePSF.

The value of the sky in the PC images is very small: about one digital unit. Because of the wider bandpass of the unfiltered STIS images and the smaller number of electrons per digital unit, the value for the sky in these images is a few tens of digital units. The sky does not vary significantly with position in an image for either the PC or STIS data. The sky level does vary between images, which probably reflects different amounts of scattered light at different points in the HST orbit. For the STIS data, the measured sky value increases with increasing flux of an object when its total flux in the science data array is larger than about  $10^4$  digital units. Above this value of the total flux, the contribution from the “tails” of the flux distribution of an object to the signal in the sky annulus becomes larger than the noise in the estimate of the sky. However, this effect is negligible since the higher skies for these bright objects are very small when compared to the total fluxes of these objects.

## 5. Construction of the ePSF

### 5.1. Selecting Objects for the Construction of the ePSF

A star, or QSO, which contributes to the construction of the ePSF must satisfy two criteria. 1. Certain specified pixels in the  $5 \times 5$  science data array must have zero flags. 2. The  $S/N$  of an object must be larger than some specified limit. Below we discuss each criterion in greater detail.

There are generally very few objects in our images that are both bright and that have all of their flags equal to zero. Experience showed that including objects that had a few pixels with non-zero flags did not significantly degrade the final result. The analysis in this article requires that the flags be equal to zero for the inner  $3 \times 3$  pixels of the science data

array.

The second criterion requires that the  $S/N$  of an object calculated with

$$S/N = \frac{\sum_{i=1}^{25} v_i}{\left(\sum_{i=1}^{25} u_i^2\right)^{1/2}} \quad (5)$$

be larger than some specified limit. Here  $v_i$  is the signal in a pixel (corrected for the sky) and  $u_i$  is the uncertainty in  $v_i$ . Both sums include only those pixels whose flags equal zero.

Trade-offs determine the value of the  $S/N$  limit. A relatively large  $S/N$  limit allows only a few very bright objects to contribute to the construction of the ePSF. The small number of contributing objects introduces noise into the ePSF due to the undersampling. Decreasing the  $S/N$  limit allows more objects to contribute, reducing the effects of undersampling, but progressively increasing the effect of photon noise on the constructed ePSF. The adopted  $S/N$  limit is the one which minimizes the uncertainties in the fitted stellar centroids of the brightest 10% of the stars. However, the final results are insensitive to the exact value of this limit. For Fornax, the limit is  $S/N = 30$ . In general, the adopted value could vary from field to field depending on the number of stars present.

Our fields have relatively few stars. For example, the master list has about 600 entries for the field with the largest number of stars and only about 100 entries for the field with the smallest. Of these, only a handful are bright stars. Thus, the scarcity of bright stars is a serious problem for the construction of the ePSF. The best sampling of the ePSF results from constructing a single ePSF per field at each epoch. For the STIS data, constructing an ePSF from either the 24 individual science images or the 8 combined images with cosmic ray rejection yields statistically indistinguishable average uncertainties of the centroids of the brightest 10% of the stars. The results in this article are for 24 images. For the PC data, the HST pipeline processing does not produce combined images and, thus, the results in the article are for all of the images.

## 5.2. Construction of the ePSF: Initial Estimate

Our method constructs a single ePSF for all of the images of a field at an epoch. The ePSF is realized on a  $25 \times 25$  grid with a spacing between grid points of  $1/5$  pixel. Bicubic spline interpolation gives the value of the ePSF between grid points. An individual grid point has indices  $\alpha$  (horizontal direction) and  $\beta$  (vertical direction). The mathematical notation for the ePSF is  $\Pi_{\alpha,\beta}$  and the notation for its normalized form is  $\hat{\Pi}_{\alpha,\beta}$ .

Each object contributing to the construction of the ePSF must satisfy the aforemen-

tioned  $S/N$  criterion and have the flags for all of the inner  $3 \times 3$  array of pixels in the science data array equal to zero. Each object contributes with the same weight, which is ensured by normalizing the data arrays of the objects according to

$$\hat{v}_i = \frac{v_i}{\sum_{j=1}^{25} v_j} \quad (6)$$

so that

$$\sum_{i=1}^{25} \hat{v}_i = 1. \quad (7)$$

In the equations,  $\hat{v}_i$  is a normalized science pixel value with an index  $i$  for a particular object. The sums include only those pixels that have flags equal to zero.

Figure 2 shows the relationship for a particular object between the  $5 \times 5$  science data array (delineated with solid lines) and the  $25 \times 25$  ePSF grid, where dots mark the grid points. A cross marks the center of each science data pixel and the slanted cross marks the centroid of the object,  $(X_0, Y_0)$ . The center of the  $25 \times 25$  ePSF grid, marked by the small open circle, coincides by definition with  $(X_0, Y_0)$  and, thus, with the slanted cross. The two grids are offset from each other by  $\vec{\delta} = (\delta_x, \delta_y)$ . Equations 8 and 9 give the components of  $\vec{\delta}$  and Figure 3 shows its relationship to other quantities discussed below.

$$\delta_x = X_0 - p + \frac{1}{2} \quad (8)$$

$$\delta_y = Y_0 - q + \frac{1}{2} \quad (9)$$

An open dashed circle centered on the center of a science data pixel in Figure 2 encloses all of the ePSF grid points to which this pixel contributes. The radius of this dashed circle is an adjustable ePSF smoothing length,  $k$ . The contribution that a science data pixel with index  $i$  makes to the ePSF at a grid point with indices  $(\alpha, \beta)$  has a weight given by

$$w_{i,\alpha,\beta} = \begin{cases} \left(1 - \frac{|\vec{s}|^2}{k^2}\right)^2 & \text{if } |\vec{s}| < k \\ 0 & \text{if } |\vec{s}| > k. \end{cases} \quad (10)$$

In the above,  $|\vec{s}|$  is the distance between the center of the science data pixel and the ePSF grid point and is given by

$$|\vec{s}| = |\vec{r} + \vec{\delta} - \vec{v}|. \quad (11)$$

Here,  $\vec{r}$  is the vector from the central ePSF grid point to the ePSF grid point  $(\alpha, \beta)$  and  $\vec{v}$  is the vector from the center of the central science data pixel to the contributing science data pixel. See Figure 3, which shows the relationship among the quantities just described.

The initial estimate of the ePSF at each grid point  $(\alpha, \beta)$  is the weighted average of the normalized values of the contributing pixels of the science data arrays:

$$\Pi_{\alpha,\beta} = \left( \sum_{\text{images}} \sum_{\text{objects}} \sum_{i=1}^{25} \hat{v}_i w_{i,\alpha,\beta} \right) / \left( \sum_{\text{images}} \sum_{\text{objects}} \sum_{i=1}^{25} w_{i,\alpha,\beta} \right). \quad (12)$$

The normalized ePSF is

$$\hat{\Pi}_{\alpha,\beta} = \frac{25 \Pi_{\alpha,\beta}}{\sum_{\mu=1}^{25} \sum_{\nu=1}^{25} \Pi_{\mu,\nu}}, \quad (13)$$

where the factor of 25 is the number of ePSF grid points per science data pixel.

At this stage, the ePSF does not have the optimal shape because: 1) the centroids of objects contributing to its construction are only initial estimates; 2) the smoothing controlled by the parameter  $k$  broadens the ePSF; and 3) the finite size of the  $5 \times 5$  science data array causes the kernel estimate of the ePSF to be too high at grid points that are closer than a smoothing length from the boundary of the grid. In addition, the summation in Equation 12 does not guarantee that the ePSF is centered properly. The following section discusses the issue of centering and the section after that returns to the first three points.

### 5.3. Construction of the ePSF: Centering

The center of the ePSF grid defines the centroid of an object fitted to the ePSF (see Figure 2). Thus, the ePSF must be centered on its grid in a repeatable way at all epochs. The construction of the ePSF described in the previous section does not enforce any centering of the ePSF. A simple way to center the ePSF is to shift the ePSF so that its largest value is at the center of the grid. However, this is not the best way to center the ePSF because the slow variation of the ePSF near its peak makes the location of the maximum particularly susceptible to noise. An alternative way is to place the “center of light” of the ePSF at the center of the grid. A weakness of this approach is that the position of the “center of light” is particularly sensitive to values of the ePSF far from the center. These values provide little information on the centroids of objects and are also affected by noise and by errors in the level of the subtracted sky. The effect of the distant grid points can be reduced by calculating a “center of light” with the largest weight for those grid values that contain the greatest amount of information about the centroid.

In simplest terms, the determination of the centroid of an object involves shifting the ePSF with respect to the science data array to minimize some quantitative measure of the difference between the values of the ePSF and of the science data pixels. Most of the information about the centroid of the object comes from the region where the ePSF varies

most rapidly, since this is where a small offset between the ePSF and the object produces the largest difference. This region is between the relatively flat inner and outer sections of the ePSF. These ideas argue that the grid points where the ePSF varies most rapidly should have the greatest influence on the location of the center of the ePSF. Thus, our algorithm centers the ePSF by forcing a weighted “center of light” to coincide with the central grid point. The weights are proportional to the derivative of a Gaussian function,

$$w(\vec{r}) = \frac{|\vec{r}|}{r_0} \exp\left(-\frac{|\vec{r}|^2}{2r_0^2}\right). \quad (14)$$

Here  $|\vec{r}|$  is the distance from the center of the ePSF grid and  $r_0$  is an adjustable parameter on the order of  $0.5 \times \text{FWHM}$  of the ePSF. Then the weighted “center-of-light” of the ePSF,  $\vec{r}_{\text{cm}}$ , is

$$\vec{r}_{\text{cm}} = \frac{\sum_{\alpha=1}^{25} \sum_{\beta=1}^{25} \vec{r}_{\alpha,\beta} w(\vec{r}_{\alpha,\beta}) \hat{\Pi}(\vec{r}_{\alpha,\beta})}{\sum_{\alpha=1}^{25} \sum_{\beta=1}^{25} w(\vec{r}_{\alpha,\beta}) \hat{\Pi}(\vec{r}_{\alpha,\beta})}. \quad (15)$$

The algorithm iteratively shifts the ePSF on the grid by  $-\vec{r}_{\text{cm}}$  using bicubic spline interpolation,

$$\Pi(\vec{r}_{\alpha,\beta} + \vec{r}_{\text{cm}}) \rightarrow \Pi(\vec{r}_{\alpha,\beta}), \quad (16)$$

until the  $x$  and  $y$  components of  $\vec{r}_{\text{cm}}$  are smaller than 0.001 pixel. Here and for the rest of this discussion we drop the “hat” notation, since by the ePSF we will now always mean its normalized form.

#### 5.4. Construction of the ePSF: Iterative Adjustments

The initial estimate of the ePSF differs from the true ePSF for the reasons described at the end of Section 5.2. Our iterative algorithm for improving the shape of the ePSF begins by deriving new, presumably more accurate, centroids by fitting the initial estimate of the ePSF to the science data arrays. An improved shape of the ePSF then results from calculating the difference between each pixel of the science data array of an object and the fitted ePSF and then calculating the weighted average of this difference at each ePSF grid point using all of the objects contributing to the ePSF. Adding this correction to the original ePSF produces a more accurate estimate. The weights are again calculated with equation 10. The difference between the fitted ePSF and the data varies more slowly than the ePSF itself and the shallower gradients reduce the bias near the boundary of the ePSF grid — the bias caused by smoothing with a kernel.

The equation that implements these corrections is

$$\Pi_{\alpha,\beta} \leftarrow \Pi_{\alpha,\beta} + \left( \sum_{\text{images}} \sum_{\text{objects}} \sum_{i=1}^{25} \frac{v_i^j - f^j \Pi(\vec{v}_i^j - \vec{\delta}^j)}{f^j} w_{i,\alpha,\beta} \right) / \left( \sum_{\text{images}} \sum_{\text{objects}} \sum_{i=1}^{25} w_{i,\alpha,\beta} \right). \quad (17)$$

In the above equation,  $f^j$  is the total fitted flux of object  $j$ . The vector  $\vec{v} - \vec{\delta}$  contains the implicit dependence of the correction on the centroid of an object. The iterative application of Equation 17 gives progressively more accurate centroids and a progressively more accurate estimate of the ePSF. Of course, noise in the science data eventually limits the usefulness of subsequent iterations. We find that the ePSF converges to a stable solution in four iterations.

The construction of the ePSF for PC data has an additional step that identifies and excludes those science data pixels which are corrupted by cosmic rays or large dark rates. The initial step is to calculate the median for the pixels in each particular location in the science data arrays of an object and to exclude those values which are more than five times the median. After one iteration of corrections has improved the ePSF, fitting the ePSF to those science data arrays contributing to the construction of the ePSF yields the expected value of each pixel and those pixels which are more than five times their uncertainties from this expected value are excluded from further consideration. The uncertainty includes both the uncertainty in the pixel value and 6% of that value, where the latter accounts for the mismatch between the constructed and true ePSF. Using the remaining pixels, the algorithm updates the list of objects contributing to the ePSF and begins the construction the ePSF anew. This process of identifying cosmic rays and constructing the ePSF anew iterates until the number of additional corrupted pixels is zero. The algorithm then continues with the iterative corrections to the ePSF as for the STIS data. In the STIS data, a few pixels with large dark rates (“hot pixels”) may not be flagged by the reduction pipeline but could be eliminated by the methods described in this paragraph. We have not found this to be necessary for our Fornax images, but we will consider it on a case-by-case basis for our other dSph data.

An additional refinement to the centroid of an object in the iterative loop applying corrections to the ePSF is to replace it with the average calculated from the centroids of the object in different images. In detail, the procedure is as follows. Find all of the objects common to the fiducial image (chosen to be the first image) and an image  $k$ . Let  $\vec{X}_i^1$  and  $\vec{X}_i^k$  be the position vectors of the centroids of the same object,  $i$ , in the fiducial and  $k$  images, respectively. Note that generally  $\vec{X}_i^1 \neq \vec{X}_i^k$  because of dithering and a possible difference in image scale and orientation. Determine the ratio of the image scales,  $s$ , offset,  $\vec{D}$ , and angle of rotation,  $\theta$ , in the transformation

$$\vec{X}^1 = s^{1,k} R(\theta)^{1,k} \times (\vec{X}^k - \vec{D}^{1,k}). \quad (18)$$

with a least-squares fit. Here  $R(\theta)$  is the solid-body rotation matrix:

$$R(\theta) = \begin{pmatrix} \cos(\theta) & \sin(\theta) \\ -\sin(\theta) & \cos(\theta) \end{pmatrix}. \quad (19)$$

Transform the centroid of an object in image  $k$  to the coordinate system of the fiducial image. Find the average centroid using the value from every image where the object satisfies the criteria for contributing to the construction of the ePSF. Transform the average centroid back to the coordinate system of image  $k$ .

The panels in Figure 4 show the ePSF resulting after four iterations for the 24 first-epoch STIS images of the FOR J0238 – 3443 field as a gray-scale map (top-left) and a contour plot (top-right) and also show its cross section along the horizontal bisector (bottom-left) and the vertical bisector (bottom-right). The levels in the contour plot are separated by 5% of the maximum value. A total of 738 science data arrays from the 24 images contributed to the construction of the ePSF (note that a given object contributes at least one and at most 24 science data arrays). Each occurrence of an object must have a  $S/N$  larger than 30 and the flags of the inner  $3 \times 3$  of the  $5 \times 5$  array of science data pixels equal to 0. The smoothing length,  $k$ , is 1 pixel and the width of the weighting function used in the centering algorithm,  $r_0$ , is 0.8 pixel. Based on experience, these values of the free parameters are close to the optimal values which yield the smallest uncertainties in the positions of objects.

Similarly, Figure 5 shows the ePSF resulting after four iterations for the 18 first-epoch PC images of the FOR J0240 – 3434 field. The panels are the same as Figure 4. A total of 513 science data arrays from the 18 images contributed to the construction of the ePSF, with each having a  $S/N$  larger than 30 and the same requirements for the flags as for Figure 4. The values for  $k$  and  $r_0$  are 1.0 pixel and 0.8 pixel, respectively.

The circular and concentric contours in the inner region of the ePSF, as depicted in the top-right panels in Figures 4 and 5, show that the ePSF is azimuthally symmetric in this region. The outer 3 – 4 contours, for which the values of the ePSF are smaller and noisier than those in the inner region, deviate from azimuthal symmetry. The outer part of the ePSF for the PC data has extensions pointing towards the four corners of the figure that are probably caused by diffraction spikes. The FWHM of the ePSF is about 1.6 pixel (or about 8 ePSF grid spacings) for the STIS data and about 1.4 pixel for the PC data. The value of the FWHM depends on the choice of the ePSF smoothing length,  $k$ . It increases with increasing  $k$ .

There is no way to tell from Figures 4 and 5 whether the depicted ePSF is the true ePSF. A way to test the algorithm that constructs and centers the ePSF is to apply it to artificial images that closely model real data. The artificial data consist of 8 images where



the dithers are the same as that for the FOR J0238 – 3443 field. The artificial field contains 962 stars located on a grid with centroids at random locations within a pixel. The values of the science data pixels are generated with a two-dimensional Gaussian distribution with a FWHM equal to 1.5 pixels in both dimensions. The noise in the images has a normal distribution and an amplitude given by the uncertainty of a pixel value in the science data array. Furthermore, we add “sky” to the images and set the flags of 3% of the pixels to a non-zero value. The latter reflects the percentage of non-zero flags in the real data.

Figure 6 shows the fractional difference between the true PSF (tPSF) and the constructed ePSF for the artificial images, after four iterations, as a function of the distance  $|\vec{r}|$  from the center of the ePSF grid. A total of 5843 science data arrays contributed to the construction of the ePSF. The smoothing length,  $k$ , is 0.5 pixel (2.5 in the units of the plot) and the width of the weighting function in the centering algorithm,  $r_0$ , is 0.8 pixel. The mean fractional difference between the tPSF and the ePSF is less than 0.5% for grid points with  $|\vec{r}| \lesssim 10$  (or about 2.0 pixels). The mean difference is small even at larger radii, but the increasing scatter in the points makes this mean uncertain. The larger scatter in the points at larger radii is a reflection of the small values of the tPSF there. The scatter in Figure 6 reflects the noise in the ePSF. The noise increases as the smoothing length decreases below 0.5 pixel. Increasing the smoothing length decreases the noise, however it also introduces systematic differences between the ePSF and tPSF as the smoothing length approaches the FWHM of a stellar image. For example, the fractional difference shows systematic trends with  $|\vec{r}|$  that are 10% or larger for  $k = 1.3$  pixel and a FWHM of 1.5 pixel. Figure 6 shows that the algorithm which generates the ePSF reproduces the tPSF if the smoothing length is not too large compared to the stellar FWHM.

Reducing the number of artificial stars contributing to the construction of the ePSF from 5843 to 128 (the latter is of the same order as the number of stars used to construct the ePSF for the real data) increases the noise in the ePSF. The noise increases both because of the smaller number of photons contributing to the ePSF and the sparser sampling of the tPSF. For  $k = 0.5$ , the mean fractional difference between the tPSF and the ePSF is again about 0% for all values of  $|\vec{r}|$ . However, the root-mean-square (*rms*) scatter is larger than that in Figure 6. It increases with increasing  $|\vec{r}|$  and is about 1% – 2% for  $|\vec{r}| \leq 5$ .

Selecting a value for the smoothing length,  $k$ , is a balance between decreasing the noise and minimizing the systematic errors in the ePSF. Its optimal value minimizes the average uncertainty in the positions of the brightest stars. The uncertainty in the position of a star is the uncertainty in the mean of the positions from the individual images as estimated from their scatter.

### 5.5. Is the ePSF for a QSO different from that for a star?

The objects contributing to the construction of the ePSF are stars and the QSO. Using the same ePSF to determine the centroids of both the stars and the QSO could produce systematic errors in the centroids if the ePSF of the QSO differs from the ePSF of a star. These systematic errors cancel out if they are the same at all epochs. The cancellation would occur if the ePSF is the same at all epochs, but this may not be the case. Indeed, our data show evidence that the ePSF can differ between epochs: the middle epoch of the FOR J0240 – 3438 field has an ePSF that varies across the image, whereas the other two epochs do not show such variability (see Section 6.1). Thus, it is necessary to explore whether the ePSF of the QSO is the same as that of a star.

Visual inspection of the images of the QSOs in our three fields in Fornax show that all appear stellar, but a quantitative comparison between the ePSF of a QSO and that of the stars might reveal more subtle differences. One such method is to construct both ePSFs and compare them. However, this method is not feasible for our data since there are too few images of a QSO to construct a well-sampled ePSF for it — the noise introduced by the undersampling dominates the comparison.

Another quantitative comparison of the two ePSFs is the  $\chi^2$  of the fit of the ePSF to the science data arrays. Section 6.1 shows that the  $\chi^2$  of the QSO does not differ significantly from those of stars with comparable brightness. However, the  $\chi^2$  is insensitive to systematic trends in the residuals resulting from subtracting the fitted ePSF from the value of each pixel in the science data array. Figure 7 plots these residuals for the stars (slanted crosses) and QSOs (solid squares and triangles) contributing to the construction of the ePSF as a function of distance from the fitted centroid,  $r$ , in units of the ePSF grid spacing. The panels show, from top to bottom, the residuals for the fiducial images of the first-epoch observations of the fields FOR J0238 – 3443 (STIS observations), FOR J0240 – 3434 (PC observations), and FOR J0240 – 3438 (STIS observations).

The distribution of the residuals for the QSO is identical to that for the stars in the top and middle panels of Figure 7. The solid squares and triangles in the middle panel correspond to the two images of the lensed QSO in this field. In contrast, the distribution of residuals for the QSO in the bottom panel is different from that for the stars. The residuals for the stars are positive near  $r = 0$  and negative near  $r = 5$ , reflecting a small mismatch between the constructed and true ePSF caused by smoothing. However, the residuals for the QSO are negative and the same at both radii. Therefore, the image of this QSO is slightly more extended than that of a star. The QSO in the FOR J0240 – 3438 field is the closest of the three,  $z = 0.38$  *versus*  $z = 2.00$  and  $1.40$  (Tinney, Da Costa, & Zinnecker 1997), and the surrounding galaxy is visible in our images. The difference between the radial profiles of the

QSO in the FOR J0240 – 3438 field and that of a star is comparable to the variation in the ePSF within a field (see Section 6.1). For this reason, the effect on the astrometry is likely to be small. Ultimately, it will be the agreement between the proper motions derived from all three fields in Fornax that will determine whether the effect on the astrometry is indeed negligible.

## 6. Determination of the Centroids of Objects

Having determined the ePSF, the algorithm fits for the centroid of object  $j$ , implicit in  $\vec{\delta}^j$ , and its total flux,  $f^j$ , by minimizing

$$\chi^2(\vec{\delta}^j, f^j) = \sum_{i=1}^{25} \left( \frac{v_i^j - f^j \Pi(\vec{v}_i - \vec{\delta}^j)}{u_i^j} \right)^2. \quad (20)$$

The best-fitting  $\vec{\delta}^j$  must be determined numerically, whereas the best-fitting  $f^j$  for a given  $\vec{\delta}^j$  can be calculated analytically from

$$f^j = \left( \sum_{i=1}^{25} \frac{v_i^j \Pi(\vec{v}_i - \vec{\delta}^j)}{(u_i^j)^2} \right) / \sum_{i=1}^{25} \left( \frac{\Pi(\vec{v}_i - \vec{\delta}^j)}{u_i^j} \right)^2. \quad (21)$$

In both of the above equations, the sum includes only those pixels that have flags equal to zero. The algorithm uses bicubic spline interpolation to evaluate  $\Pi(\vec{v}_i - \vec{\delta}^j)$  from the tabulated ePSF grid values, where the vector  $\vec{v}_i - \vec{\delta}^j$  points from the centroid of the object  $j$  (which is also the center of the ePSF grid) to the center of science data pixel  $i$ . Equations 8 and 9 determine the centroid of an object,  $\vec{X} \equiv (X_0, Y_0)$ , from  $\vec{\delta}^j$ .

The error in a measured centroid has contributions from the noise in the constructed ePSF, a possible systematic mismatch between the constructed and true ePSF, and the noise in the science data arrays. The remainder of this section addresses the importance of these sources of error by examining: 1) how well the constructed ePSF matches the science data arrays of objects both as a function of position within the image and, when averaged over all objects, as a function of position within the science data array; 2) whether the difference between the centroids measured for an object in the individual images of an epoch depend on the the location of the object with respect to the pixel boundaries in each image; and 3) if the *rms* scatter of the centroids from the individual images depends on the location of the object within the field and on the brightness of the object.

The discussion draws on examples taken from the STIS images of the FOR J0238 – 3443 field and the PC images of the FOR J0240 – 3434 field. However, the conclusions apply to

all of our data for Fornax. The plots presented in this section are for the fiducial first-epoch STIS or PC images or for all of the first-epoch STIS or PC images.

### 6.1. Performance of the Fitting Algorithm: Flux Residual Diagnostics

This section examines the flux residuals resulting from subtracting the fitted ePSF from the values in the science data array. A dependence of these flux residuals on location within the field would indicate a spatially varying ePSF. If the flux residuals for a star produce a  $\chi^2$  of low probability, then either the uncertainties of the values in the science data array are underestimated or there is a statistically significant mismatch between the constructed ePSF and the true ePSF. A systematic mismatch could also cause some of the flux residuals averaged over all objects to be non-zero and to vary within the science data array.

The left and right panels in Figure 8a plot the mean flux residual divided by its uncertainty,

$$\mathcal{RF} = \sum_{i=1}^{25} \frac{v_i - f\hat{\Pi}(\vec{v}_i - \vec{\delta})}{u_i}, \quad (22)$$

for each object in the fiducial STIS image as a function of  $X_0$  and  $Y_0$ , respectively. The solid square is the QSO and the pluses are the objects contributing to the construction of the ePSF (which include the QSO for this image). Figure 8b is the corresponding plot for the PC image. The solid square and triangle are images A and B, respectively, of the lensed QSO. Because  $\mathcal{RF}$  is sensitive to the sign of the residuals, whereas  $\chi^2$  is not,  $\mathcal{RF}$  contains additional information on how the fitted ePSF and the science data array differ. For our data,  $\mathcal{RF}$  is a better diagnostic of variability of the ePSF with position in our fields than is  $\chi^2$ .

Figure 8a shows no discernible correlation between  $\mathcal{RF}$  and the location of an object in the image. The mean  $\mathcal{RF}$  is close to zero, though negative, and the departure from zero is statistically significant. A difference between the shapes of the constructed and true ePSF causes the average  $\mathcal{RF}$  to be non-zero. For example, Figure 10 will show that the constructed ePSF is broader than the true ePSF in the central region of the ePSF grid. The scatter of  $\mathcal{RF}$  around its mean is on the order of 0.17 and the size of the scatter does not correlate with either  $X_0$  or  $Y_0$ . The pluses tend to have a larger scatter than the points because, in Equation 22, the bright stars have smaller fractional uncertainties in  $v_i$ . They also tend to have a positive  $\mathcal{RF}$  for  $X_0 \lesssim 400$  pixels. This pattern is present in all of our STIS data for Fornax to a variable degree and is particularly conspicuous for the middle epoch of the FOR J0240 – 3438 field. We conclude that the ePSF is variable within our STIS images, though the variability is barely detectable in most of them.

The corresponding plots for the fiducial PC image, Figure 8b, show that  $\mathcal{RF}$  varies with position in the image. Unlike Figure 8a, the distribution of the pluses is similar to that of the points. This similar distribution for the bright and faint objects is a consequence of the smaller total fluxes in the PC images: the Poisson noise is larger than the systematic mismatch between the ePSF and the science data array. The typical  $\mathcal{RF}$  for the corners of the image is greater than that near the center — again, a pattern exhibited to a variable degree in all of our PC data for Fornax. Thus, as for the STIS data, the ePSF varies within the field — though the pattern of the variation is different and the amplitude of the variation is larger.

Figure 9a plots  $\chi^2$ , calculated from Equation 20, for each object in the fiducial STIS image as a function of the flux. Here the flux is the sum of all values in the science data array that have flags equal to zero. Since the summation in Equation 20 is over 25 science data pixels (less than 25 if there are pixels with non-zero flags), the  $\chi^2$  per object should be around 25. The figure shows that the value of  $\chi^2$  is about 25 for those objects with fluxes less than about  $3 \times 10^3$  counts. For higher fluxes, the  $\chi^2$  increases with flux. For example, the total  $\chi^2$  for the QSO is several hundred. Such large values for  $\chi^2$  are not necessarily alarming since, for very bright objects, the fractional uncertainties in the values in the science data array are very small and a large  $\chi^2$  does not imply large differences between the array values and the ePSF.

Figure 9b is the corresponding plot of  $\chi^2$  *versus* total flux for each object in the fiducial PC image. The trend of increasing  $\chi^2$  with flux is less apparent because of the lower fluxes and more variable ePSF in the PC image as compared to the STIS image.

Figure 8 shows that the values of  $\mathcal{RF}$  for the QSOs in fields FOR J0238 – 3443 and FOR J0240 – 3434 are similar to those for the bright stars, which is consistent with the conclusion of Section 5.5 that the images of these QSOs are indistinguishable from that of a star. In contrast, the QSO in field FOR J0240 – 3438 has a positive value of  $\mathcal{RF}$  that tends to be larger than that for any bright star. Its larger value of  $\mathcal{RF}$  is also consistent with the conclusion of Section 5.5 that the radial profile of this QSO is slightly more extended than that of a star. For all of the three fields in Fornax, the values of  $\chi^2$  for the QSO are not markedly different from those for the bright stars. Though the  $\chi^2$  of the QSO is one of the largest, if not the largest, it is comparable to the  $\chi^2$  of stars with a similar flux. Thus, the  $\chi^2$  is not a good indicator of small differences between the images of a QSO and a star because the  $\chi^2$  values of bright stars are also large.

Figure 10 explores the reason for the large  $\chi^2$  values for bright stars by showing the mean flux residual as a function of position within the science data array for all of the STIS images. The top number in a square tile is the mean over all objects of the fractional

difference between the value of the science data pixel and the fitted value, defined by

$$\langle \Delta v_i / v_i \rangle = \frac{1}{N} \sum_{j=1}^N \frac{v_i^j - f^j \Pi(\vec{v}_i - \vec{\delta}^j)}{f^j \Pi(\vec{v}_i - \vec{\delta}^j)}. \quad (23)$$

Here  $j$  is the index of an object and  $N$  is the total number of objects in the sum. The bottom number in a square tile is the mean over all objects of the difference between the value of the science data pixel and the fitted value divided by the uncertainty in the pixel value, calculated from

$$\langle \Delta v_i / u_i \rangle = \frac{1}{N} \sum_{j=1}^N \frac{v_i^j - f^j \Pi(\vec{v}_i - \vec{\delta}^j)}{u_i^j}. \quad (24)$$

The values of  $\langle \Delta v_i / v_i \rangle$  in Figure 10 are positive in the inner  $3 \times 3$  pixels and tend to be negative in those outside. This pattern supports the idea that the smoothing in the construction of the ePSF causes the constructed ePSF to be broader than the true ePSF. In the critical central  $3 \times 3$  region, the fractional difference between the ePSF and true PSF is 5% or less. In the less critical outer region, where the ePSF is small, the difference can be as large as 10%. These numbers are typical of those for our STIS and PC data for Fornax.

The largest value of  $\langle \Delta v_i / u_i \rangle$  occurs for the central pixel. A total of 8538 central pixels contribute to this average value, so, if there is no difference between the constructed ePSF and the true ePSF and the uncertainties in the array values are realistic, then the typical  $\langle \Delta v_i / u_i \rangle$  would be  $\pm 0.011$ . Thus, the largest  $\langle \Delta v_i / u_i \rangle$  is statistically significant. Likewise, the values of  $\langle \Delta v_i / u_i \rangle$  in the other tiles are statistically significant. Ideally, the values of  $\langle \Delta v_i / u_i \rangle$  would be zero, indicating a perfect match between the constructed ePSF and true ePSF. The non-zero values again arise from the smoothing imposed during the construction of the ePSF. Reducing the smoothing reduces the systematic differences between the constructed ePSF and true ePSF, but it increases the random differences. Both random and systematic differences lead to errors in the fitted centroids. We choose the smoothing which minimizes the total uncertainty in the fitted centroids.

## 6.2. Average Centroids of Objects

Let  $(X_0, Y_0)$  be the coordinates of the centroid of an object in an image expressed in the coordinate system of the fiducial image. If there are  $N$  images, there are up to  $N$  values of  $(X_0, Y_0)$  for a given object – less if that object is not fitted in some images. Let  $(\langle X_0 \rangle, \langle Y_0 \rangle)$  be the mean centroid of an object expressed in the coordinate system of the fiducial image. The residual of an  $(X_0, Y_0)$  value for an object from the  $(\langle X_0 \rangle, \langle Y_0 \rangle)$  is

$$\mathcal{R}\mathcal{X} \equiv \langle X_0 \rangle - X_0 \quad (25)$$

$$\mathcal{R}\mathcal{Y} \equiv \langle Y_0 \rangle - Y_0. \quad (26)$$

The *rms* scatter of  $X_0$  and  $Y_0$  around  $\langle X_0 \rangle$  and  $\langle Y_0 \rangle$ , respectively, are measures of how well the algorithm determines the centroid of the object.

The positions of objects on the STIS and on the WFPC2 detectors do not reflect their true positions in the sky due to geometrical distortion present in the instrument, which makes the image scale vary across the detector. The effect of this distortion on the centroid of an object can be reduced because the relationship between the true centroid of an object,  $(x_t, y_t)$ , and its measured centroid,  $(x, y)$ , with respect to the center of the CCD detector has been approximately characterized by Brown et al. (2002) for STIS and Baggett et al. (2002) for WFPC2 and is given by

$$x_t = C_0 + C_1x + C_2y + C_3x^2 + C_4xy + C_5y^2 + C_6x^3 + C_7yx^2 + C_8xy^2 + C_9y^3 \quad (27)$$

$$y_t = D_0 + D_1x + D_2y + D_3x^2 + D_4xy + D_5y^2 + D_6x^3 + D_7yx^2 + D_8xy^2 + D_9y^3. \quad (28)$$

The second and third columns of Table 2 list the coefficients for the STIS detector and the fourth and fifth columns do the same for the PC detector. These corrections are applied to all of our measured centroids before calculating the means and residuals described above. In addition to the above geometrical distortions, the WFPC2 CCD chip has a “34-th row defect” (Shaklan, Sharman, & Pravdo 1995) which introduces errors into the measured values of both the  $y$  coordinate of the centroid and the total flux of an object. Anderson & King (1999) determined corrections for these errors. Our algorithm uses their recipe (their Equation 2) to correct the errors in the  $y$  coordinates of the centroids. However, it does not correct the values of the science data array (their Equation 1) because we think that the flat-field correction performed by the HST pipeline eliminates the need for this correction for astrometric purposes.

### 6.3. Performance of the Fitting Algorithm: Position Residual Diagnostics

The two left-hand panels in Figure 11 plot the *rms* scatter of  $X_0$  (top) and  $Y_0$  (bottom) around their means *versus* the inverse of the  $S/N$  for all objects with at least two measured centroids in the first-epoch STIS images. The  $S/N$  is calculated from Equation 5. The two right-hand panels are the same for objects in the first-epoch PC images. The plots in Figure 11 are typical of our data for Fornax. The plots show a nearly linear trend of increasing *rms* scatter with increasing inverse  $S/N$ , as is expected from the uncertainties in the least-squares fit (*e.g.*, Kuijken & Rich 2002). The trend does not go through the origin in any of the plots, demonstrating that one or more sources of error that are independent of the  $S/N$  limit the accuracy of the fitted centroids for the brightest objects. The additional source

of error is likely a dependence of the measured centroid on the location of the true centroid within a pixel – called pixel-phase error by Anderson & King (2000). Pixel-phase errors arise because of a mismatch between the constructed and true ePSF. Intentional degradation of the ePSF by including fewer stars in its generation produces a larger non-zero intercept in the equivalent of Figure 11. Even an ePSF constructed from many objects can have some mismatch if the true ePSF varies across an image and Figure 8 shows that this is the case for our Fornax data. Additional mismatch can arise if the ePSF varies among images at a given epoch because of a variable size of the guiding jitter. Our data has too few stars to model the variations of the ePSF within and between images without introducing larger errors in the ePSF from undersampling. Thus, unavoidable pixel-phase errors cause the minimum *rms* of about 0.01 pixel, independent of  $S/N$ , seen in Figure 11.

The left-hand panels in Figure 12 plot, from top to bottom,  $\mathcal{RX}$  versus the decimal part of the  $X$  component of the centroid — the pixel phase  $\Phi_x$ ,  $\mathcal{RY}$  versus the decimal part of the  $Y$  component of the centroid — the pixel phase  $\Phi_y$ ,  $\mathcal{RX}$  versus  $\Phi_y$ , and  $\mathcal{RY}$  versus  $\Phi_x$ . All of the panels are for objects contributing to the construction of the ePSF for the first-epoch STIS images. The right-hand panels show the same quantities for objects in the first-epoch PC images. The plots of  $\mathcal{RX}$  versus  $\Phi_x$  and  $\mathcal{RY}$  versus  $\Phi_y$  for the STIS images probably show systematic trends in the residuals that reflect pixel-phase errors with an amplitude of about 0.01 pixel. The points for the QSO show the pixel-phase errors most clearly:  $\mathcal{RX}$  tends to be negative for  $\Phi_x \lesssim 0.5$  and positive above 0.5 and the opposite pattern is present for  $\mathcal{RY}$  versus  $\Phi_y$ . The two plots of the cross-dependences do not show any trends.

The plots for the PC images show no clear evidence for pixel-phase errors. However, if these errors depend on the position within an image, as they might because of the variation of the ePSF for the PC images implied by Figure 8, a plot for the entire region of all images will tend to show scatter instead of a trend.

#### 6.4. Uncertainty of the Average Centroid

The uncertainty of the average centroid is the *rms* scatter around the mean divided by the square root of the effective number of measurements. Estimating the uncertainty of the average centroid is complicated by the presence of pixel-phase errors. When these errors make the largest contribution to the uncertainty of the measured centroid, as they do for the brightest few objects in our sample (see Figure 11), the effective number of measurements is the number of dither positions rather than the total number of measurements of the centroid. Because pixel-phase errors cannot be eliminated from our data, we have chosen to include



their effect on the uncertainty of the mean centroid,  $\sigma_{\langle X_0 \rangle}$  or  $\sigma_{\langle Y_0 \rangle}$ , with the ad-hoc formula

$$\sigma_{\langle X_0 \rangle, \langle Y_0 \rangle} = \frac{\sigma_{X_0, Y_0}}{\left( (\sigma_0 / \sigma_{X_0, Y_0})^2 N_d + \left( 1 - (\sigma_0 / \sigma_{X_0, Y_0})^2 \right) N_{obs} \right)^{1/2}}. \quad (29)$$

Here  $\sigma_{X_0, Y_0}$  is the *rms* scatter around  $\langle X_0 \rangle$  or  $\langle Y_0 \rangle$ ,  $\sigma_0$  is the minimum uncertainty due to pixel-phase errors,  $N_d$  is the number of dither positions, and  $N_{obs}$  is the number of measurements of the centroid. From Figure 11, the value of  $\sigma_0$  is 0.013. The value of  $\sigma_0$  ranges from 0.012 to 0.013 for the Fornax data.

## 7. Determination of Proper Motion and Space Velocity

### 7.1. The Measured Proper Motion

The average centroid of an object at a given epoch is in the coordinate system of the fiducial image for this epoch. The centroid differs between epochs both because of changes in the pointing of the telescope and the proper motion of the dSph. Determining the proper motion from centroids of objects at different epochs requires adopting a standard coordinate system tied to the stars of the dSph. These stars determine a transformation between the coordinate system of the fiducial image at the later epoch and the fiducial image at the earlier epoch.

The transformation to the standard coordinate system has a similar form to the one given in Equation 18:

$$\vec{X}^{tr}(t_2) = sR(\theta) \times \left( \vec{X}(t_2) - \vec{X}_Q(t_2) \right) - \vec{X}_Q^{tr}(t_2). \quad (30)$$

The transformation coefficients result from varying the plate scale,  $s$ , angle,  $\theta$ , and the transformed coordinates of the QSO,  $(X_Q^{tr}(t_2), Y_Q^{tr}(t_2))$ , to minimize

$$\chi^2 = \sum_{i=1}^N \left( \frac{(X_i(t_1) - X_i^{tr}(t_2))^2}{\sigma_{X_i(t_1)}^2 + \sigma_{X_i^{tr}(t_2)}^2} + \frac{(Y_i(t_1) - Y_i^{tr}(t_2))^2}{\sigma_{Y_i(t_1)}^2 + \sigma_{Y_i^{tr}(t_2)}^2} \right). \quad (31)$$

Here the uncertainties of the transformed centroids are given by

$$\sigma_{X_i^{tr}(t_2)} = s \left( \cos^2(\theta) \sigma_{X_i(t_2)}^2 + \sin^2(\theta) \sigma_{Y_i(t_2)}^2 \right)^{1/2} \quad (32)$$

$$\sigma_{Y_i^{tr}(t_2)} = s \left( \sin^2(\theta) \sigma_{X_i(t_2)}^2 + \cos^2(\theta) \sigma_{Y_i(t_2)}^2 \right)^{1/2}. \quad (33)$$

The objects that determine the transformation are those with a  $S/N$  above some limit, which is 20 for the Fornax data. The QSO is excluded from the determination of the transformation,

as is every object whose change in position between epochs is more than 2.5 times, for STIS, or 4.5 times, for the PC, its uncertainty. The set of excluded objects is determined iteratively, with the iteration ceasing when the set stops changing. The number of excluded objects is at most 15% of a sample of 60 or more objects. The final proper motion does not depend sensitively on the limits that determine the sample which defines the transformation. A typical change in scale between epochs is a few parts per 100,000 and the typical angle of rotation is on the order of a few thousandths of a degree or less.

The uncertainty in the transformed coordinates,  $(X^{tr}(t_2), Y^{tr}(t_2))$ , depends on both the uncertainty in the measured centroid,  $(X(t_2), Y(t_2))$ , and on the uncertainty in the transformation. For the QSO, these uncertainties are independent and should be added in quadrature. Even for the objects that contributed to the determination of the transformation, adding the two uncertainties in quadrature is a reasonable procedure as long as the sample of objects is at least a few tens.

The contribution to the uncertainty in  $(X^{tr}(t_2), Y^{tr}(t_2))$  from the uncertainty in the coefficients of the transformation could be estimated by varying the coefficients so that  $\chi^2$  increases from its minimum value by one — see the discussion in Chapter 15 of Press et al. (1992). Because implementing this estimate is very complex, we have adopted a simpler and more intuitive approach. The values of  $(X_Q^{tr}(t_2), Y_Q^{tr}(t_2))$  that minimize  $\chi^2$  are

$$X_Q^{tr}(t_2) = \left( \sum_{i=1}^N \frac{X_i(t_1) - s((X_i(t_2) - X_Q(t_2)) \cos(\theta) - (Y_i(t_2) - Y_Q(t_2)) \sin(\theta))}{\sigma_{X_i(t_1)}^2 + \sigma_{X_i^{tr}(t_2)}^2} \right) / \left( \sum_{i=1}^N \frac{1}{\sigma_{X_i(t_1)}^2 + \sigma_{X_i^{tr}(t_2)}^2} \right) \quad (34)$$

and

$$Y_Q^{tr}(t_2) = \left( \sum_{i=1}^N \frac{Y_i(t_1) - s((X_i(t_2) - X_Q(t_2)) \sin(\theta) - (Y_i(t_2) - Y_Q(t_2)) \cos(\theta))}{\sigma_{Y_i(t_1)}^2 + \sigma_{Y_i^{tr}(t_2)}^2} \right) / \left( \sum_{i=1}^N \frac{1}{\sigma_{Y_i(t_1)}^2 + \sigma_{Y_i^{tr}(t_2)}^2} \right). \quad (35)$$

Applying propagation of errors to the above equations yields the following uncertainties for the two parameters:

$$\sigma_{X_Q^{tr}(t_2)} = \left( \sum_{i=1}^N \frac{1}{\sigma_{X_i(t_1)}^2 + \sigma_{X_i^{tr}(t_2)}^2} \right)^{-1/2} \quad (36)$$

$$\sigma_{Y_Q^{tr}(t_2)} = \left( \sum_{i=1}^N \frac{1}{\sigma_{Y_i(t_1)}^2 + \sigma_{Y_i^{tr}(t_2)}^2} \right)^{-1/2}. \quad (37)$$

The above estimates for the contribution from the transformation to the uncertainty in  $(X^{tr}(t_2), Y^{tr}(t_2))$  are accurate if the covariances of the parameters in the transformation are small, which is the case if the number of objects determining the transformation is much larger than the number of parameters and the objects are widely distributed in the field. The data for Fornax satisfies these requirements. The uncertainties in the transformed coordinates of objects other than the QSO also have contributions from the uncertainties in  $s$  and  $\theta$ . We neglect these additional contributions in the calculation of the uncertainties since they do not directly affect the measured proper motion of the dSph. Thus, the uncertainty in the centroid from the later epoch transformed into the coordinate system of the first epoch is the measurement uncertainty of the later-epoch centroid added in quadrature to the uncertainty arising from the transformation, given by Equations 36 and 37.

As defined in Section 3,  $p_x$  and  $p_y$  are the components of the difference between the two centroids of an individual object, measured at different epochs, in the standard coordinate system. The two panels in Figure 13 plot the uncertainty in  $p_x$ ,  $\sigma_{p_x}$ , (top) and the uncertainty in  $p_y$ ,  $\sigma_{p_y}$ , (bottom) *versus* the inverse of the average  $S/N$ . The figures in this section use the epoch 2000 and 2001 data for the FOR J0238 – 3443 field. The  $S/N$  is from the earlier epoch. The plots show the expected approximate linear increase of  $\sigma_{p_x}$  and  $\sigma_{p_y}$  with decreasing  $S/N$ . The smallest uncertainty in the change in a centroid ( $p_x$  or  $p_y$ ) is about 0.005 pixel. This uncertainty is comparable to that necessary to measure the proper motion of a typical dSph, as estimated in Section 1.

The panels in Figure 14 show how the values of  $p_x$  and  $p_y$  depend on location for objects with a  $S/N$  greater than 30. Figure 13 shows that this limit corresponds to an uncertainty in  $p_x$  or  $p_y$  of less than approximately 0.01 pixel. The two left-hand panels plot  $p_x$  (top) and  $p_y$  (bottom) *versus*  $X(t_1)$ . The two right-hand panels similarly plot the same quantities *versus*  $Y(t_1)$ . None of the panels in Figure 14 shows a trend with either  $X(t_1)$  or  $Y(t_1)$ . The absence of trends argues that the form of the transformation to the standard system is adequate and that any variation of the ePSF across the image does not affect significantly  $p_x$  and  $p_y$  and, thus, does not affect the measured proper motion.

A figure analogous to Figure 14 for the PC data for field FOR J0240 – 3434 shows that  $p_x$  and  $p_y$  depend on  $X(t_1)$  and  $Y(t_1)$ , respectively, with a pattern that resembles the one for  $\mathcal{RF}$  in Figure 8b. The dependence of  $p_x$  and  $p_y$  on location argues that the ePSF changed enough between epochs to introduce systematic errors in the proper motion. Adding terms depending on  $X^2$  and  $Y^2$  to the transformation, Equation 30, reduces, but does not completely eliminate this dependence. The two values for the  $X$  component of the proper motion derived using the two images of the QSO in this field differ by about twice the uncertainty in their difference. The two  $Y$  components agree within their uncertainties. We

increase the uncertainties in both the  $X$  and  $Y$  components of the measured proper motions for this field to reflect the remaining systematic errors. The uncertainties are equal to each other and have a value that makes the difference in the two measured  $X$  components of the proper motion equal to its uncertainty.

Figure 15 plots  $p_y$  versus  $p_x$  for the same objects as in Figure 14. The distribution of points is centered on and isotropic about the origin, as is expected for stars of Fornax. The solid square representing the QSO is clearly offset from the origin and its error bars indicate that this offset is about twice its uncertainty. Figure 16, which plots  $p_y/\sigma_{p_y}$  versus  $p_x/\sigma_{p_x}$ , shows that the QSO has one of the most significant offsets from the origin. A  $2\sigma$  offset is not a significant detection of the proper motion of Fornax, however these data have a time baseline of only one year. Our measurements for three fields, two of which have baselines of two years, do produce a significant detection.

Multiplying  $-p_{Q,x}$  and  $-p_{Q,y}$  by the image scale and dividing by the time baseline between the two epochs yields the components of the proper motion of Fornax in the standard coordinate system,  $\mu_x$  and  $\mu_y$ . Rotating the coordinate system using the known position angle of the  $Y$  axis of the standard coordinate system gives the measured  $\mu_\alpha$  and  $\mu_\delta$  in the equatorial coordinate system. Table 3 gives these measured quantities for the three fields in the direction of the Fornax dSph in units of milliarcseconds per century. These components of the proper motion are those that are measured on the sky without applying corrections for the motions of the Sun and the LSR. The following section applies the appropriate corrections and uses the results to calculate the velocity of Fornax in various reference frames.

## 7.2. Galactic-Rest-Frame Proper Motion in the Equatorial Coordinate System

The measured proper motion includes the effects of the motion of the LSR and the peculiar motion of the Sun with respect to the LSR. Both motions must be removed from the measured proper motion to obtain the proper motion of a dSph in the Galactic rest frame. Let  $(\mu_\alpha^{\text{LSR}}, \mu_\delta^{\text{LSR}})$  and  $(\mu_\alpha^\odot, \mu_\delta^\odot)$  be the contributions to the measured proper motion from the motion of the LSR and the peculiar motion of the Sun, respectively. The components of the rest-frame proper motion of the dSph in the equatorial coordinate system are then given by

$$\mu_\alpha^{\text{Grf}} = \mu_\alpha - \mu_\alpha^{\text{LSR}} - \mu_\alpha^\odot \quad (38)$$

$$\mu_\delta^{\text{Grf}} = \mu_\delta - \mu_\delta^{\text{LSR}} - \mu_\delta^\odot. \quad (39)$$

The corrections due to the motion of the LSR are (Mihalas & Binney 1981)

$$\mu_\alpha^{\text{LSR}} = \frac{\Theta_0 \sin(\lambda) \sin(\psi)}{4.741 d} \quad (40)$$

$$\mu_{\delta}^{\text{LSR}} = -\frac{\Theta_0 \sin(\lambda) \cos(\psi)}{4.741 d}. \quad (41)$$

Here  $\Theta_0$  is the circular velocity of the LSR with respect to the Galactic center,  $220 \text{ km s}^{-1}$ ,  $\lambda$  is the angular distance between the dSph and the apex of the motion of the LSR, and  $\psi$  is the angle between two great circles, one passing through the dSph and the North Celestial Pole (NCP) and the other passing through the dSph and the apex. The quantity  $d$  is the heliocentric distance to the dSph in pc.

Replacing  $\Theta_0$  with  $\mathcal{V}_{\odot} = (u_{\odot}^2 + v_{\odot}^2 + w_{\odot}^2)^{\frac{1}{2}}$ , where  $(u_{\odot}, v_{\odot}, w_{\odot})$  are the components of the solar motion with respect to LSR, and redefining the angles  $\lambda$  and  $\psi$  to be with respect to the apex of the solar motion, equations 40 and 41 also give  $(\mu_{\alpha}^{\odot}, \mu_{\delta}^{\odot})$ . The  $u_{\odot}$  component of the solar motion is positive if it points radially away from the Galactic center; the  $v_{\odot}$  component is positive if it is in the direction of rotation of the Galactic disk; and the  $w_{\odot}$  component is positive if it is in the direction of the North Galactic Pole (NGP). In this work  $(u_{\odot}, v_{\odot}, w_{\odot}) = (-10.0, 5.25, 7.17) \pm (0.36, 0.62, 0.38) \text{ km s}^{-1}$  (Dehnen & Binney 1998).

### 7.3. Galactic Coordinate System

The components of the proper motion in the galactic coordinate system,  $(\mu_l, \mu_b)$ , are

$$\mu_l = \mu_{\alpha} \cos(\eta) + \mu_{\delta} \sin(\eta) \quad (42)$$

$$\mu_b = -\mu_{\alpha} \sin(\eta) + \mu_{\delta} \cos(\eta), \quad (43)$$

where  $\eta$  is an angle between two great circles intersecting at the location of dSph on the sky. One great circle passes through the dSph and the NCP and the other great circle passes through the dSph and the NGP. The value of  $\eta$  can be calculated from a spherical triangle whose vertices are at the dSph, NCP, and NGP using standard spherical trigonometry. The sign of  $\eta$  is positive if, upon going around this triangle from the dSph through the NCP and the NGP, the triangle is on the left (Smart 1977).

### 7.4. Space Velocity of a dSph in the LSR and Galactic Rest Frames

Let  $(u, v, w)$  be the components of the space velocity of a dSph with respect to the LSR. In this coordinate system,  $u$  is positive if it points radially away from the Galactic center;  $v$  is positive if it is in the direction of Galactic rotation; and  $w$  is positive if it is in the direction of the NGP. These directions are all defined at the location of the LSR. The

$(u, v, w)$  components are given by

$$u = -v_r \cos(b) \cos(l) + \mu_b d \sin(b) \cos(l) + \mu_l d \sin(l) + u_\odot \quad (44)$$

$$v = v_r \cos(b) \sin(l) - \mu_b d \sin(b) \sin(l) + \mu_l d \cos(l) + v_\odot \quad (45)$$

$$w = v_r \sin(b) + \mu_b d \cos(b) + w_\odot. \quad (46)$$

Here  $v_r$  is the heliocentric radial velocity of the dSph.

We define a similar cylindrical coordinate system at the location of the dSph to express the components of the velocity of the dSph with respect to the Galactic center,  $(\Pi, \Theta, Z)$ . In this coordinate system,  $\Pi$  is parallel to the plane of the Galactic disk and is positive in the direction away from the Galactic center. The velocity components are given by,

$$\Pi = u \cos(\beta) + (v + \Theta_0) \sin(\beta) \quad (47)$$

$$\Theta = -u \sin(\beta) + (v + \Theta_0) \cos(\beta) \quad (48)$$

$$Z = w, \quad (49)$$

where  $\beta$  is the angle between the line connecting the Galactic center and the origin of the LSR and the line connecting the Sun and a point corresponding the projection of the dSph onto the Galactic plane.

## 8. Results

Table 3 lists the measured proper motion of the Fornax dSph galaxy determined in each of three fields. The two measurements for the FOR J0240 – 3434 field are for the two images of the lensed QSO. The three measurements for the three pairs of epochs for the FOR J0240 – 3438 field have the same set of high proper motion stars rejected in the determination of the coordinate transformation between epochs. The first and last epoch determine the set of stars rejected since this pair of epochs produces the most accurate proper motions. The first column of the table gives the name of the field; the second column gives the two epochs for which the third and fourth columns give the components in the J2000.0 equatorial coordinate system of the measured proper motion in  $\text{mas cent}^{-1}$ :  $\mu_\alpha$  and  $\mu_\delta$ , respectively. These values of the proper motion do not include any corrections for the solar motion or for the motion of the LSR; they are as-measured on the sky. The bottom line of Table 3 gives the weighted average of  $\mu_\alpha$  and of  $\mu_\delta$  and their corresponding uncertainties.

The values of  $\mu_\alpha$  and  $\mu_\delta$  for the FOR J0238 – 3443, FOR J0240 – 3434, and FOR J0240 – 3438 fields represent independent measurements of the proper motion of Fornax. The two measured proper motions for the two images of the lensed QSO in the FOR J0240 – 3434

field are not completely independent since the measurements share the transformation into the fiducial coordinate system. However, the uncertainties in the  $p_x$  and  $p_y$  of each image of the lensed QSO are much larger than the uncertainties in the transformation, so we consider these two measurements to be independent.

The tabulated uncertainties for  $\mu_\alpha$  and  $\mu_\delta$  for the FOR J0240–3434 field are about twice as large as those given by the uncertainty in  $p_{Q,x}$  and  $p_{Q,y}$  to account for the remaining dependence of  $p_x$  and  $p_y$  on location. The tabulated uncertainties result from the uncertainties in  $\mu_x$  and  $\mu_y$  described in Section 7.1.

### 8.1. Galactic-Rest-Frame Proper Motion of Fornax

The third and fourth columns of Table 4 give the proper motion of Fornax in the Galactic rest frame,  $\mu_\alpha^{\text{Grf}}$  and  $\mu_\delta^{\text{Grf}}$  respectively, determined in the three fields. This rest-frame proper motion assumes a distance to Fornax of 138 kpc (Mateo 1998). The first two columns of Table 4 are the same as those for Table 3. The corresponding values of  $\mu_l^{\text{Grf}}$  and  $\mu_b^{\text{Grf}}$  are in the fifth and sixth columns, respectively. The next three columns are the  $\Pi$ ,  $\Theta$ , and  $Z$  components of the velocity of Fornax with respect to the Galactic center (see Equations 47, 48, and 49). These values additionally assume a distance between the Sun and the Galactic Center of 8.5 kpc and a heliocentric radial velocity for Fornax of  $53 \pm 3 \text{ km s}^{-1}$  (Mateo 1998). The final two columns give the radial and tangential velocities of Fornax with respect to the Galactic center. The bottom line of Table 4 gives the weighted average for the tabulated quantities and their corresponding uncertainties.

The three values for the rest-frame proper motion of Fornax derived from the three pairs of epochs available for the FOR J0240 – 3438 field agree within their uncertainties. The remainder of the article uses the value of the proper motion for the longest baseline. We will derive the proper motion using all three epochs for each field once we have the complete set of data for Fornax.

The FOR J0238 – 3443 and FOR J0240 – 3434 fields and the 2000→2002 baseline for the FOR J0240 – 3438 field yield four independent measurements of the proper motion of Fornax. The weighted mean of the magnitudes of the four rest-frame proper motion vectors is  $48 \pm 13 \text{ mas cent}^{-1}$ . The chi-square of the scatter around this mean is 0.41 for 3 degrees of freedom, a value which should be exceeded 94% of the time by chance. The weighted mean position angle of the rest-frame proper motion vector and its uncertainty are  $145 \pm 15$  degrees. The  $\chi^2$  of the scatter around this mean is 1.3 for 3 degrees of freedom, a value which should be exceeded 73% of the time by chance. Thus, the four independent measurements of the

proper motion agree within their uncertainties.

The position angle of the major axis of Fornax is  $48 \pm 6$  degrees (Mateo 1998). Thus, the rest-frame proper motion is nearly along the minor axis. The average Galactocentric radial and tangential velocities in Table 4 show that the orbital motion of Fornax is nearly across our line of sight. Thus, Fornax is not elongated along its orbit.

## 8.2. Galactic Orbit of Fornax

The values for the average  $\Pi$ ,  $\Theta$ , and  $Z$  in Table 4 show that Fornax has a retrograde and moderately inclined Galactic orbit. The small size of the Galactocentric radial velocity compared to the tangential velocity implies that Fornax is near apogalacticon or perigalacticon. We estimate a value of the apo- and perigalacticon for the logarithmic potential of the Milky Way given by

$$\Phi(R) = \frac{1}{2} \Theta_0^2 \ln \left( \frac{R}{R_0} \right), \quad (50)$$

where  $R_0$  is the current Galactocentric radius of Fornax. Using the conservation of energy and of angular momentum, the above equation can be rewritten as

$$\ln \left( \frac{R_m}{R_0} \right) = \left( \frac{V_r}{\Theta_0} \right)^2 + \left( \frac{V_t}{\Theta_0} \right)^2 \left( 1 - \left( \frac{R_0}{R_m} \right)^2 \right). \quad (51)$$

Here  $V_r$  and  $V_t$  are the current Galactocentric radial and tangential velocities of Fornax, respectively, and  $R_m$  is either the apogalacticon,  $R_a$ , or the perigalacticon,  $R_p$ . For  $V_r = -40 \text{ km s}^{-1}$  and  $V_t = 310 \text{ km s}^{-1}$ ,  $R_p = 0.99 R_0$  and  $R_a = 7.2 R_0$ . Such a large apogalacticon argues that Fornax is not bound to the Milky Way. Note, however, that decreasing  $V_t$  by  $1\sigma$  reduces  $R_a$  to  $2.6 R_0$ , while  $R_p$  remains practically unchanged, and that a circular orbit ( $V_r = 0$ ,  $V_t = 220 \text{ km s}^{-1}$ ) is consistent with the measured values. The plausible range of values for  $V_r$  and  $V_t$  imply a space velocity larger than the assumed Galactic circular velocity, demonstrating that Fornax is close to perigalacticon.

## 8.3. A Lower Limit for the Mass of the Milky Way

If Fornax is bound gravitationally to the Milky Way, its Galactocentric velocity provides a lower limit on the mass of the Galaxy. If the gravitational potential of the Milky Way is spherically symmetric, then the lower limit on its mass,  $\mathcal{M}$ , is

$$\mathcal{M} = \frac{R(V_r^2 + V_t^2)}{2G}, \quad (52)$$



where  $R$  is the Galactocentric radius of the dSph. Substituting in the average values for the velocities and  $R = 140$  kpc gives  $\mathcal{M} = (1.6 \pm 0.8) \times 10^{12} \mathcal{M}_{\odot}$ . The stated uncertainty in this limit comes from the uncertainty in the velocity of Fornax.

#### 8.4. Is Fornax a Member of a Stream?

The location of the Draco, Sculptor, and Ursa Minor dSphs on the great circle of the Magellanic Stream (Lynden-Bell 1976; Kunkel & Demers 1977), the alignment of the major axes of Draco and Ursa Minor with this great circle (Lynden-Bell 1983), and the possible correlation of the positions of other dSphs and globular clusters with and the alignment of their major axes along great circles in the sky (*e.g.*, Lynden-Bell 1994, Majewski 1994, Lynden-Bell & Lynden-Bell 1995) suggest the presence of coherent streams in the Galactic halo. Lynden-Bell & Lynden-Bell (1995) proposed membership for Fornax in four possible streams and predicted its proper motion for each case. Since the other proposed members of these streams are at smaller Galactocentric radii than Fornax, the large perigalacticon of Fornax found in Section 8.2 argues against the reality of these four streams. The predicted proper motions are in the same quadrant as the average value in Table 3, however, the magnitude of the measured proper motion vector is larger than the predictions by factors of 1.7 to 3.8. The discrepancy between the predicted and our measured proper motion is more than  $2\sigma$ .

Lynden-Bell (1982; see also Majewski 1994) also proposed that Fornax could be a member of a stream with the Leo I, Leo II, and Sculptor dSphs. The direction of our measured rest-frame proper motion is 52 degrees from the great circle containing Fornax, Leo I, and Leo II. The discrepancy between the directions is more than three times the uncertainty in the position angle of the rest-frame proper motion vector.

### 9. Summary

This article describes our method for measuring proper motions of dSph galaxies from dithered images taken with HST at multiple epochs, each of which contains at least one previously-known QSO. The steps in this method are: construct an ePSF from the bright objects in the images, fit the ePSF to all of the objects to determine their accurate centroids, and transform the centroids to a common coordinate system. The measured proper motion of a dSph is the average shift of the positions of its stars with respect to the QSO.

The construction of a well-sampled ePSF is central to our method. Ideally, the ePSF

would have the freedom to vary from image to image and to vary within an image. However, because there are relatively few stars with sufficiently high  $S/N$  in our fields, constructing a well-sampled ePSF requires using a single, constant ePSF for a field at each epoch. This limitation introduces an error that depends on the location of the centroid within a pixel and limits the accuracy of a measured centroid to 0.013 pixel for a single image. Averaging the centroids from images at eight independent dither positions yields a proper motion accurate to about  $35 \text{ mas cent}^{-1}$  for a pair of epochs separated by 1 year. This accuracy is sufficient to measure the proper motion of the Fornax dSph galaxy.

We present four independent measurements of the proper motion of Fornax based on data from three different fields taken with two different detectors — STIS and PC. These measurements agree within their uncertainties, lending credibility to the method and the measured value.

The average measured proper motion of Fornax is  $\mu_\alpha = 49 \pm 13 \text{ mas cent}^{-1}$  and  $\mu_\delta = -59 \pm 13 \text{ mas cent}^{-1}$ . The average proper motion vector corrected for the motion of the Sun and LSR (the proper motion in the Galactic rest frame) has a magnitude of  $48 \pm 13 \text{ mas cent}^{-1}$  and a position angle of  $145 \pm 15$  degrees. This position angle places the rest-frame proper motion vector approximately along the minor axis of Fornax. Fornax has Galactocentric radial and tangential velocities of  $-40 \pm 50 \text{ km s}^{-1}$  and  $310 \pm 80 \text{ km s}^{-1}$ , respectively. Assuming that the Galaxy has a flat rotation curve with a circular velocity of  $220 \text{ km s}^{-1}$ , Fornax is near perigalacticon and, unless its space velocity is about  $1\sigma$  or more below the measured value, it reaches such large Galactocentric radii that it is bound to the Local Group rather than to the Galaxy. If Fornax is bound to the Galaxy, the implied lower limit on the mass of the Milky Way is  $(1.6 \pm 0.8) \times 10^{12} \mathcal{M}_\odot$ .

Our measured proper motion for Fornax precludes its membership in the proposed Fornax-Leo-Sculptor stream or in any of the streams proposed in Lynden-Bell & Lynden-Bell (1995).

CP and SP acknowledge the financial support of the Space Telescope Science Institute through the grants HST-GO-07341.03-A and HST-GO-08286.03-A. EWO acknowledges support from the Space Telescope Science Institute through the grants HST-GO-07341.01-A and HST-GO-08286.01-A and from the National Science Foundation through the grants AST-9619524 and AST-0098518. MM acknowledges support from the Space Telescope Science Institute through the grants HST-GO-07341.02-A and HST-GO-08286.02-A and from the National Science Foundation through the grant AST-0098661. HM acknowledges support from the National Science Foundation through the grant AST-0098435. DM is supported by FONDAP Center for Astrophysics 15010003.

## REFERENCES

- Anderson, J. & King, I. R. 1999, *PASP*, 111, 1095
- Anderson, J. & King, I. R. 2000, *PASP*, 112, 1360
- Baggett, S. et al. 2002, in *HST WFPC2 Data Handbook*, v 4.0, ed. B. Mobasher, Baltimore, STScI
- Bedin, L. R., Anderson, J., King, I. R., & Piotto, G. 2001, *ApJ*, 560, L75
- Bernstein, G. 2002, *PASP*, 114, 98
- Brown, T., et al. 2002, in *HST STIS Data Handbook*, version 4.0, ed. B. Mobasher, Baltimore, STScI
- Cudworth, K. M., Olszewski, E. W., & Schommer, R. A. 1986, *AJ*, 92, 766
- Dehnen, W., & Binney, J. J. 1998, *MNRAS*, 298, 387
- King, I. R., Anderson, J., Cool, A. M., & Piotto, G. 1998, *ApJ*, 492, L37
- Kuijken, K., & Rich, R. M. 2002, *astro-ph/0207116*
- Kunkel, D. E., & Demers, S. 1977, *ApJ*, 214, 21
- Lauer, T. R. 1999, *PASP*, 111, 1434
- Lynden-Bell, D. 1976, *MNRAS*, 174, 695
- Lynden-Bell, D. 1982, *Observatory*, 102, 202
- Lynden-Bell, D. 1983, in *Internal Kinematics and Dynamics of Galaxies*, IAU Symp. 100, ed. E. Athanassoula (Dordrecht: Reidel), 89
- Lynden-Bell, D. 1994, in *Dwarf Galaxies*, ESO/OHP Workshop Proceedings No. 49, ed. G. Meylan & P. Prugniel (Garching: ESO), 589
- Lynden-Bell, D., & Lynden-Bell, R. M. 1995, *MNRAS*, 275, 429
- Majewski, S. R. 1994, *ApJ*, 431, L17
- Mateo, M. 1998, *ARAA*, 36, 435
- Monet, D. G.; Dahn, C. C., Vrba, F. J., Harris, H. C., Pier, J. R., Luginbuhl, C. B., & Ables, H. D. 1992, *AJ*, 103, 638
- Scholtz, R. -D. & Irwin, M. J. 1993 in *IAU Symp. 161, Astronomy from Wide-Field Imaging*, ed. H. T. MacGillivray et al. (Dordrecht: Kluwer), p. 535
- Press, W. H., Teukolsky, S. A., Vetterling, W. T., & Flannery, B. P. 1992, *Numerical Recipes* (Cambridge, Cambridge Univ. Press)
- Shaklan, S., Sharman, M. C., & Pravdo, S. H. 1995, *Appl. Opt.*, 34, 6672

- Stetson, P. B. 1987, *PASP*, 99, 191
- Stetson, P. B. 1992, in *ASP Conf. Ser. Vol. 25, Astronomical Data Analysis Software and Systems*, ed. D. M. Worrall, C. Biemesderfer, & J. Barnes (San Francisco: ASP), 297
- Stetson, P. B. 1994, *PASP*, 106, 250
- Schweitzer, A. E., Cudworth, K. M., & Majewski, S. R. 1997, in *ASP Conf. Ser. 127, Proper Motions and Galactic Astronomy*, ed. R. M. Humphreys (San Francisco: ASP), 132
- Smart, W. M. 1997, *Textbook on Spherical Astronomy* (Cambridge: Cambridge University Press)
- Tinney, C. G. 1995, *MNRAS*, 277, 609
- Tinney, C. G. 1996, *MNRAS*, 281, 644
- Tinney, C. G., Da Costa, G. S., & Zinnecker, H. 1997, *MNRAS*, 285, 111
- Tinney, G. G., Reid, I. N., Gizis, J., & Mould, J. R. 1995, *AJ*, 110, 3014
- van den Bergh, S. 2000, *The Galaxies of the Local Group*, Cambridge Astrophysics Series No. 35 (Cambridge: Cambridge University Press)

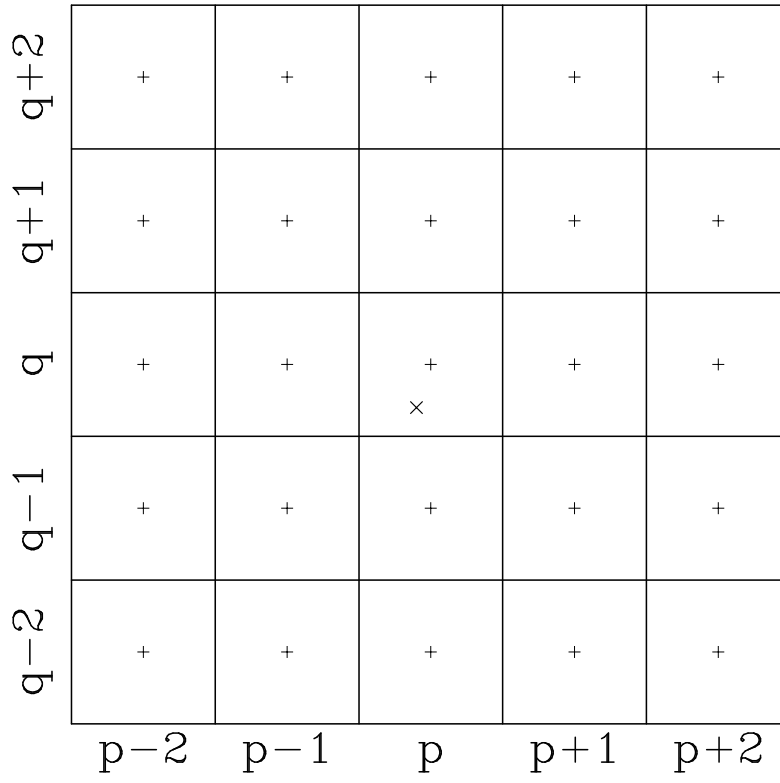


Fig. 1.— The  $5 \times 5$  array of science data pixels extracted for each object. A plus marks the center of a pixel and the slanted cross marks the centroid of an object.

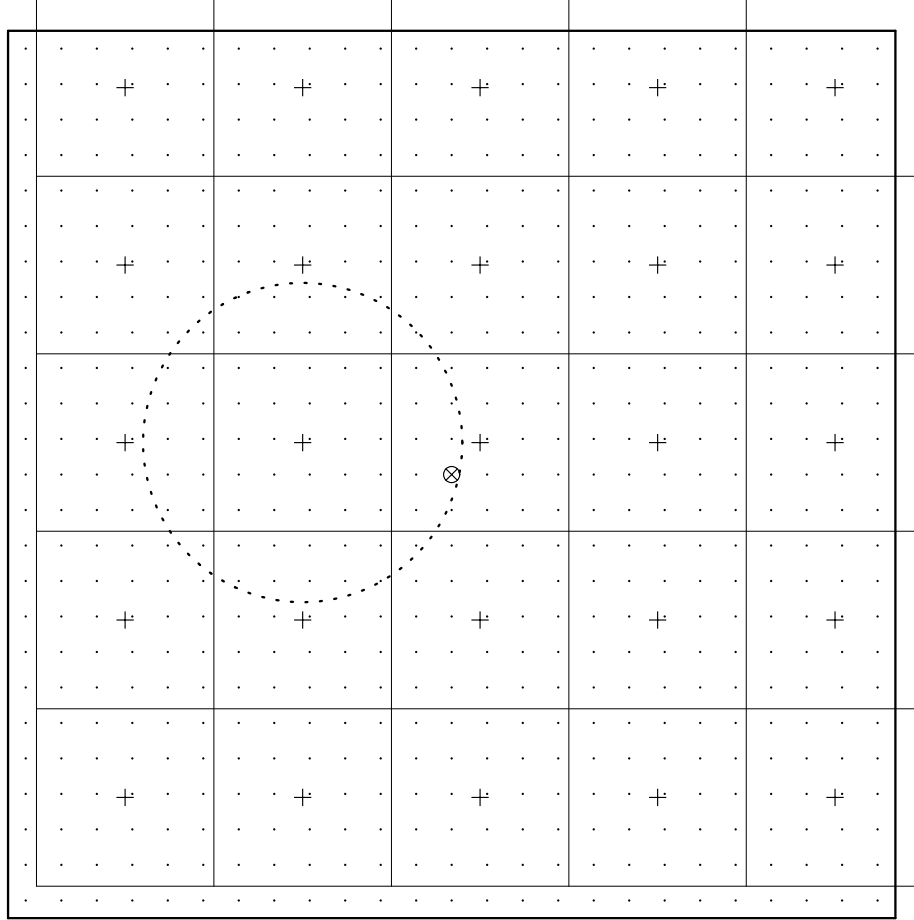


Fig. 2.— The solid  $5 \times 5$  grid represents the science data array for a particular object. A cross marks the center of each science data pixel. The slanted cross marks the centroid of the object. The  $25 \times 25$  array of dots represents the points at which the ePSF is realized. The center of the ePSF grid, marked with an open circle, coincides by definition with the centroid of the object. Since the centroid of an object can be anywhere within the central pixel in the  $5 \times 5$  grid, the two grids are offset by  $\vec{\delta}$ , whose magnitude is equal to the distance between the centroid of the object and the center of the central science data pixel. The open dashed circle encloses those ePSF grid points to which the science data pixel on which the circle is centered contributes. The radius of the dashed circle is an adjustable parameter,  $k$ , referred to as the ePSF smoothing length.

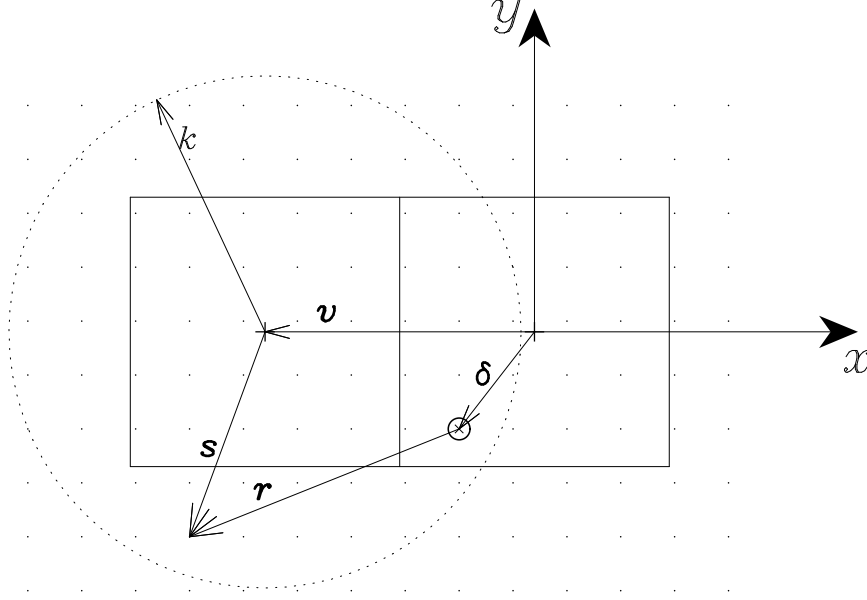


Fig. 3.— The figure shows a relationship among the quantities involved in the construction of the ePSF. The two solid squares are science data pixels: the central pixel, whose center defines the origin of a local  $x$ - $y$  coordinate system, and an adjacent one which is contributing to the ePSF grid point. The pluses mark their centers. The dots represent the ePSF grid points. The center of the ePSF, marked with an open circle, coincides with the centroid of the object, marked with the slanted cross. The science data pixel with the position vector  $\vec{v}$  contributes to the ePSF grid point with the position vector  $\vec{r}$ . The contribution is weighted, where the weight depends on the length of vector  $\vec{s}$  and is calculated from Equation 10. The science data pixel contributes to all of the ePSF grid points contained in the dashed circle, whose radius is equal to the adjustable smoothing length,  $k$ . From the figure, it follows that  $\vec{\delta} + \vec{r} = \vec{v} + \vec{s}$ . Note that  $\vec{v}$  is not always horizontal and it should not be confused with  $v$ , which denotes a science data pixel value.

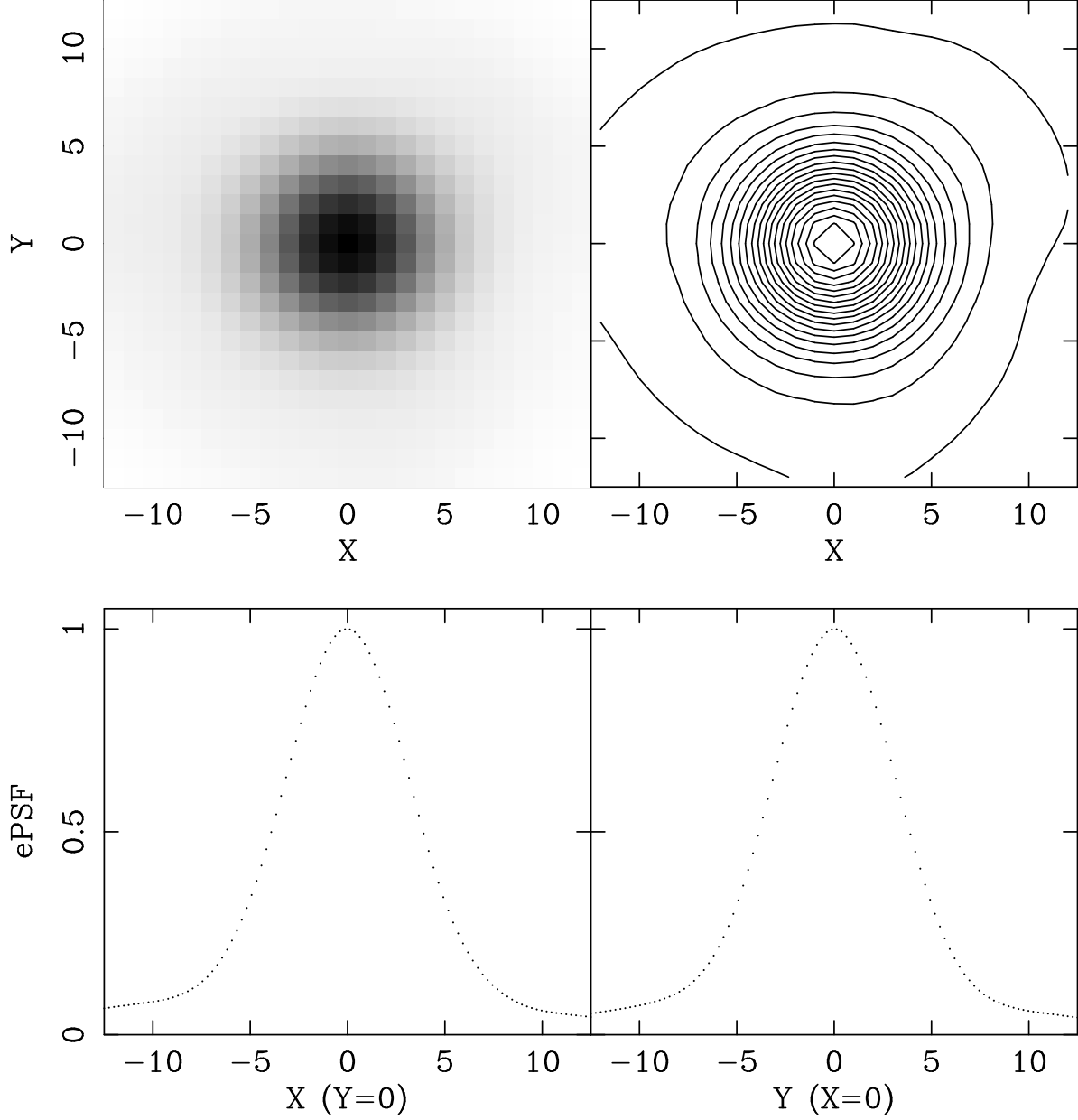


Fig. 4.— The ePSF after four iterations for the 24 first-epoch STIS images of the FOR J0238 – 3443 field. Top-left panel: Gray-scale map of the ePSF. Top-right panel: Contour plot of the ePSF; the levels are separated by 5% of the maximum value. Bottom-left panel: ePSF values along the horizontal bisector. Bottom-right panel: ePSF values along the vertical bisector.



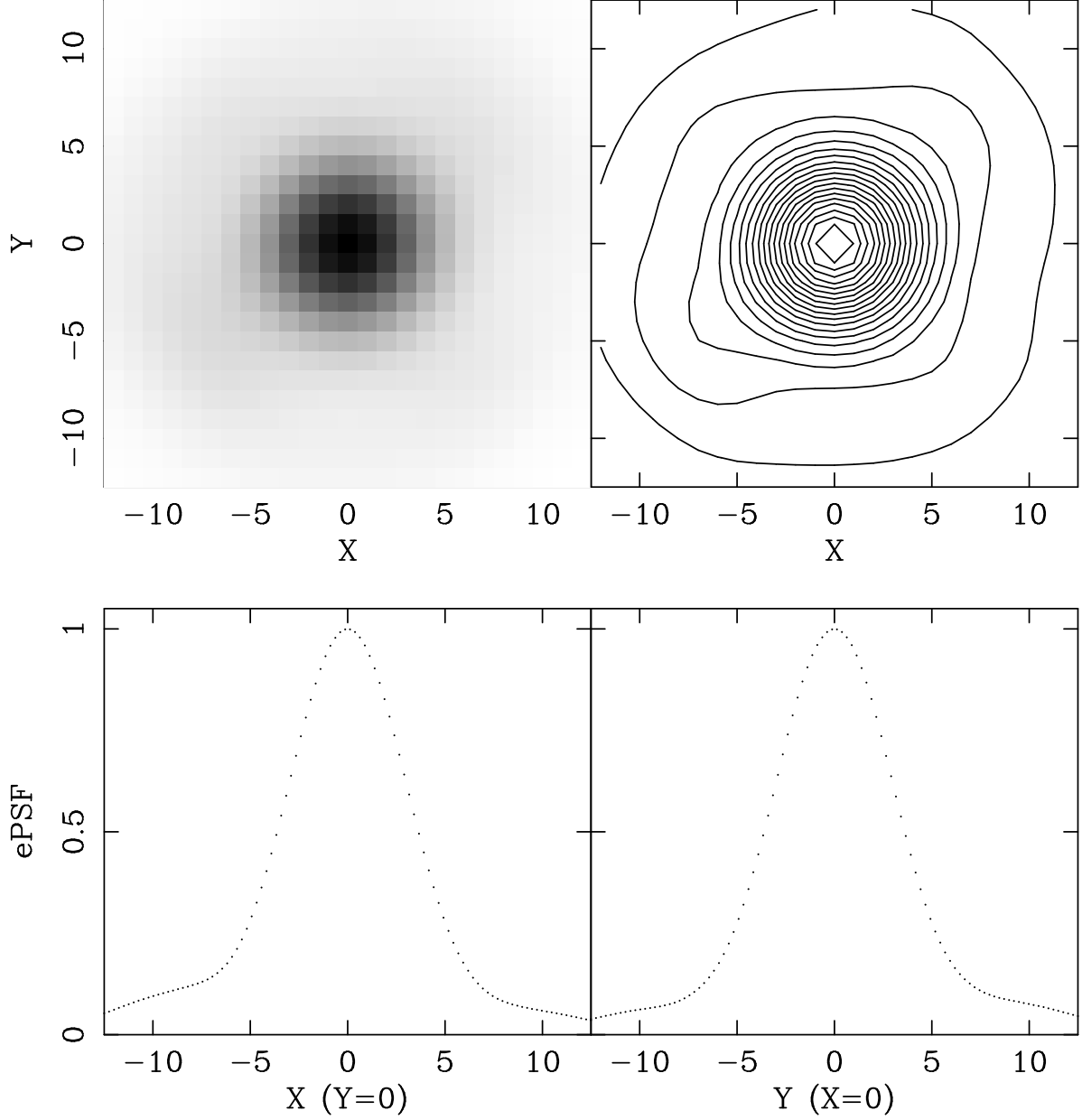


Fig. 5.— The ePSF after four iterations for the 18 first-epoch PC images of the FOR J0240–3434 field. Top-left panel: Gray-scale map of the ePSF. Top-right panel: Contour plot of the ePSF; the levels are separated by 5% of the maximum value. Bottom-left panel: ePSF values along the horizontal bisector. Bottom-right panel: ePSF values along the vertical bisector.

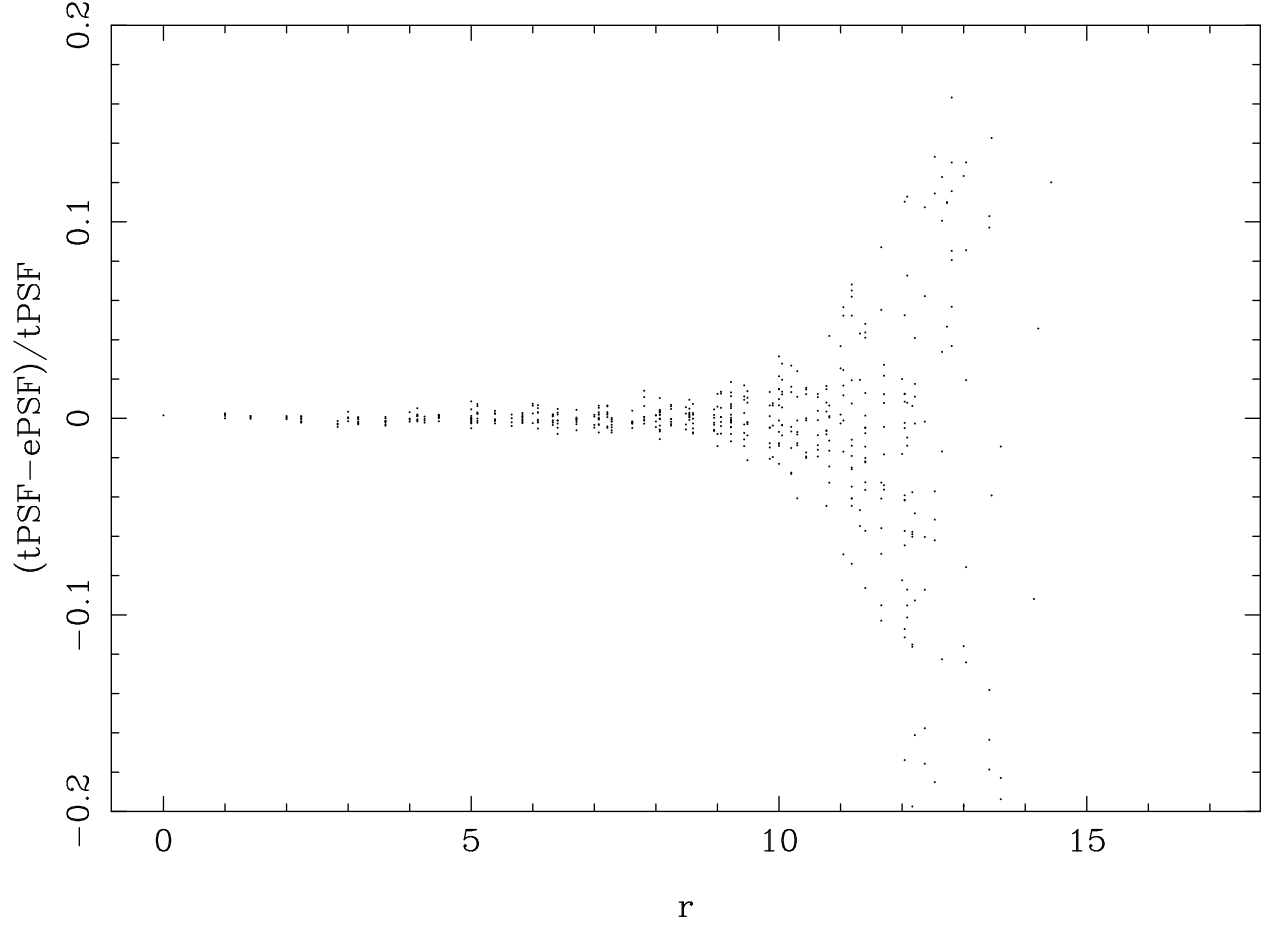


Fig. 6.— The fractional difference between the true PSF (tPSF) and the constructed ePSF, after four iterations, as a function of the distance from the center of the ePSF grid. The tPSF is a two-dimensional Gaussian function with a FWHM of 1.5 pixels in both directions. Note that 1.0 pixel is five times the spacing of the ePSF grid — the grid spacing is the unit of distance in the plot.

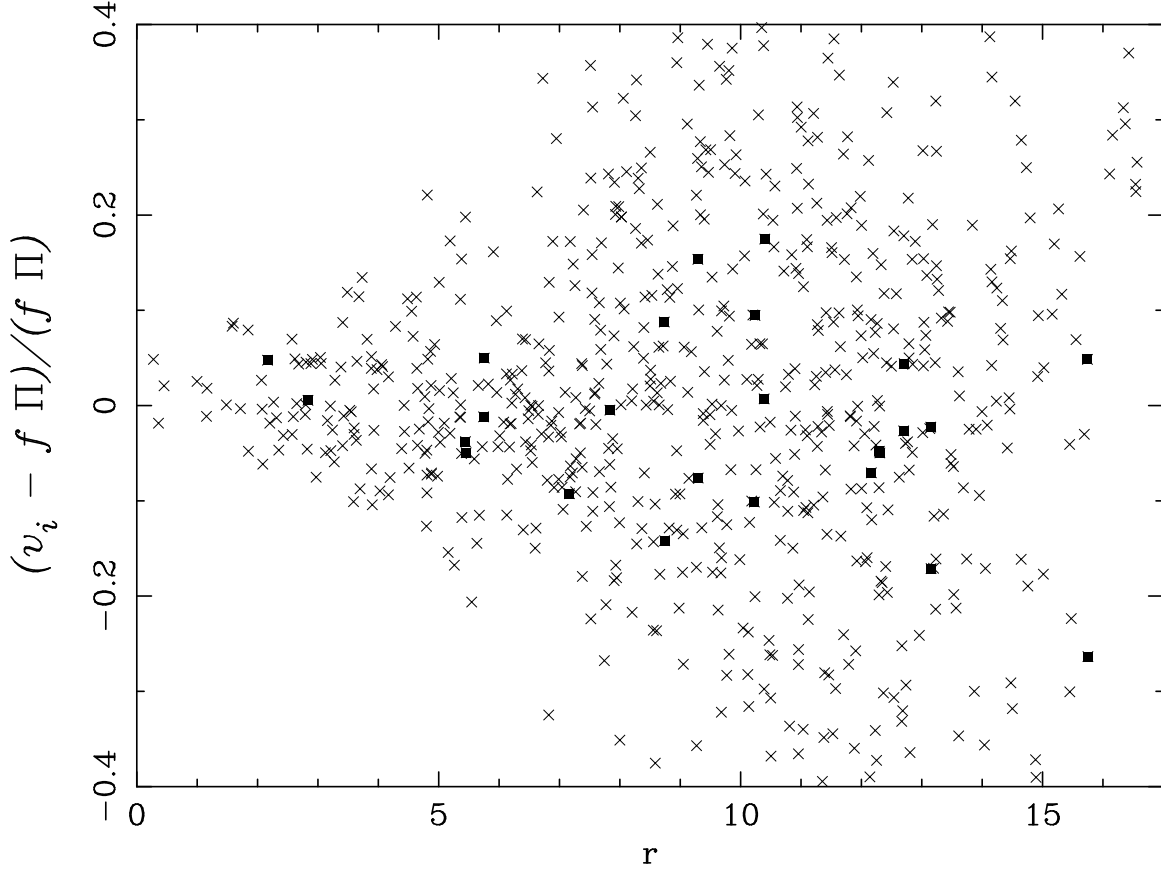


Fig. 7.— a) The residuals resulting from subtracting the fitted ePSF from the value of each pixel in the science data array plotted *versus* the distance from the fitted centroid in units of the ePSF grid spacing. Only data for objects contributing to the construction of the ePSF appear. The slanted crosses are the residuals for the stars and the solid squares are the residuals for the QSO for the fiducial image, taken with STIS, of the first epoch observations of the FOR J0238 – 3443 field.

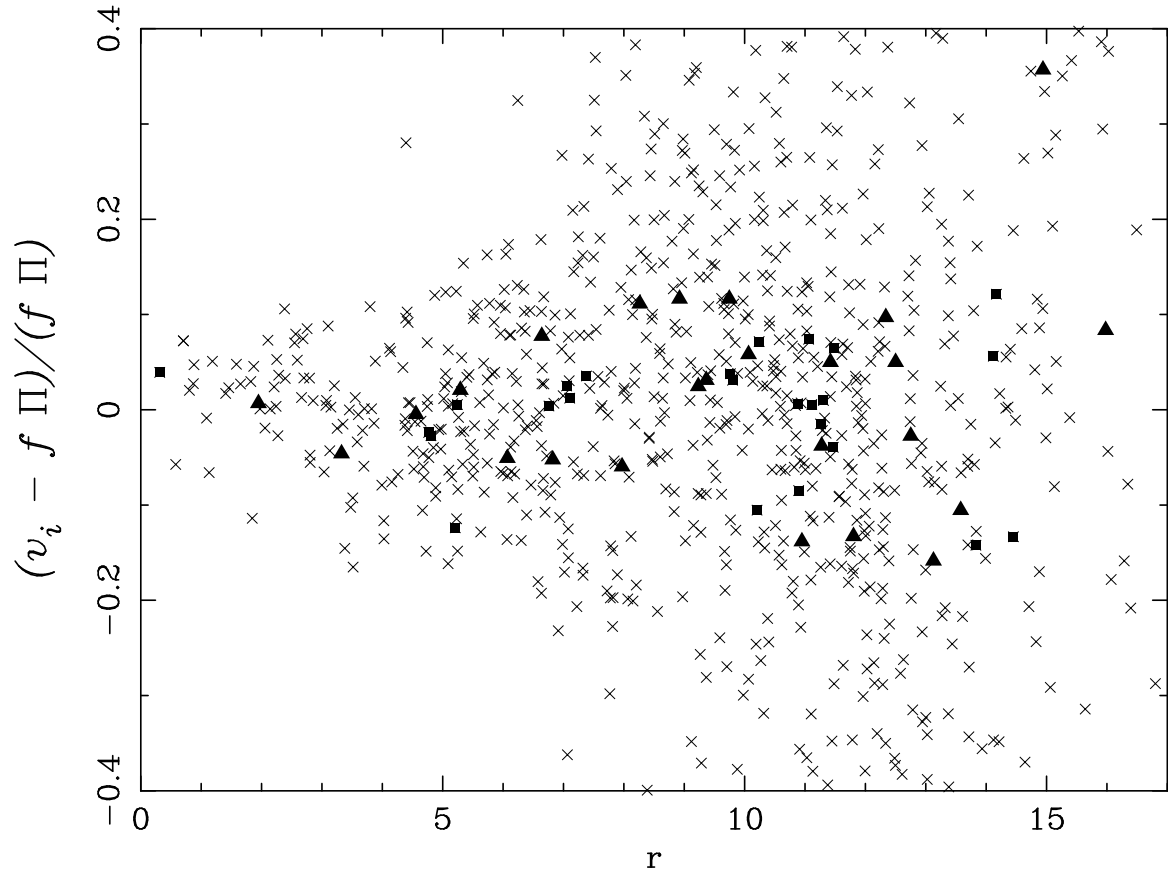


Fig. 7.— b) The same as a) for the fiducial image, taken with the PC, for the FOR J0240 – 3434 field. The solid triangles represents the points for the second image of the lensed QSO.

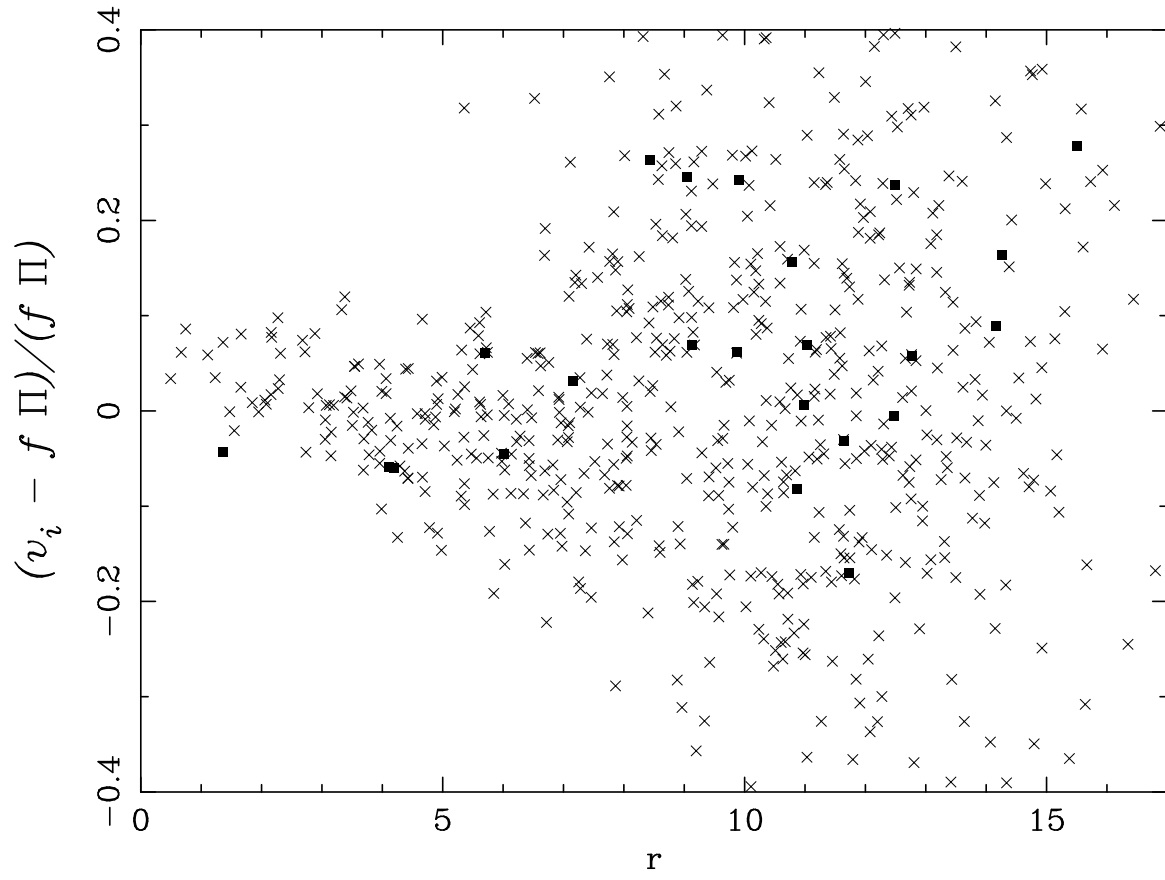


Fig. 7.— c) The same as a) for the FOR J0240 – 3438 field.

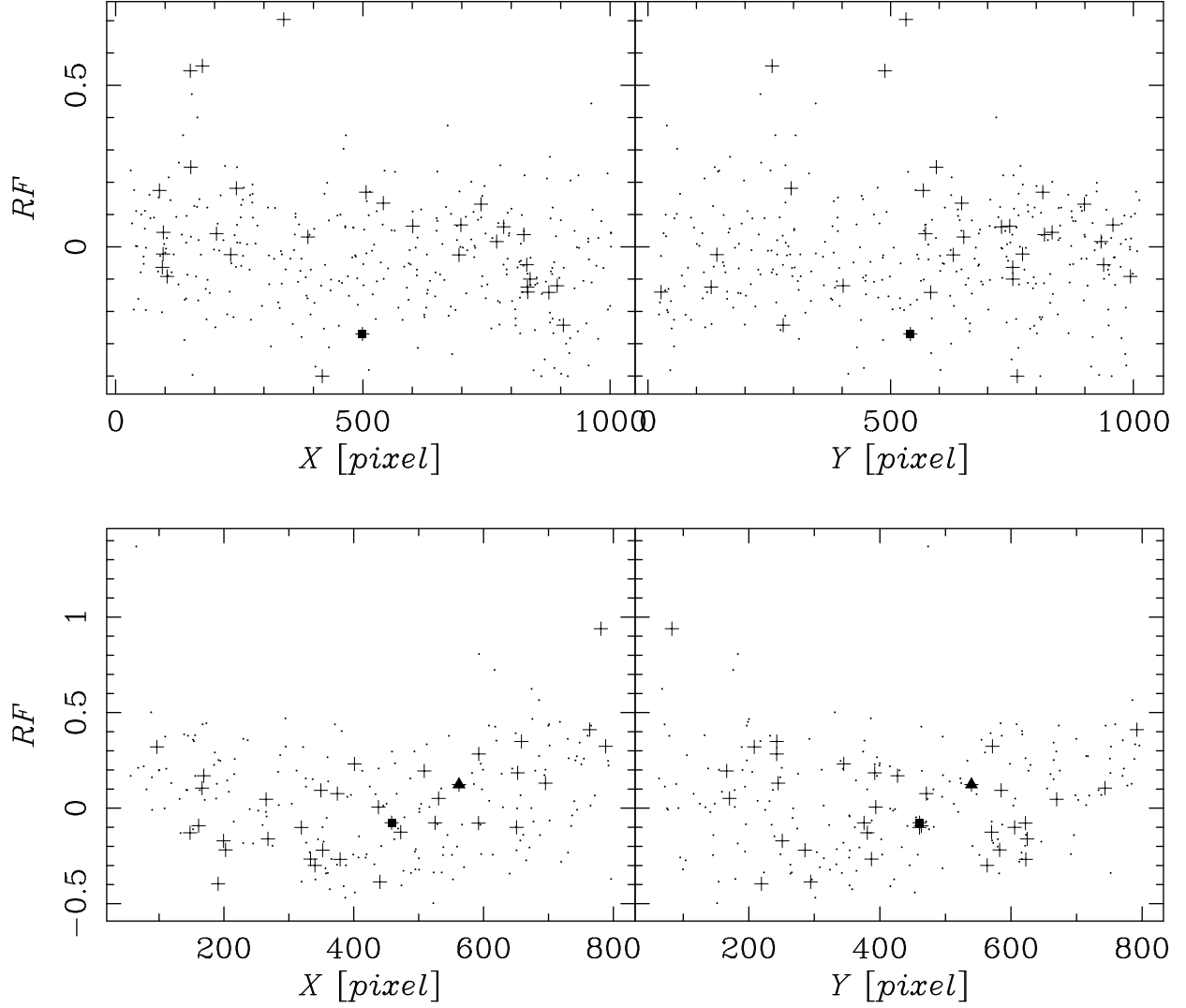


Fig. 8.— a) The left and right panels plot the mean flux residual,  $\mathcal{RF}$ , for each object in the fiducial STIS image as a function of  $X_0$  and  $Y_0$ , respectively. The solid square is the QSO and the pluses are the objects contributing to the construction of the ePSF (which include the QSO for this image). b) The same plots for the fiducial PC image. The solid square and triangle correspond to images A and B, respectively, of the lensed QSO.

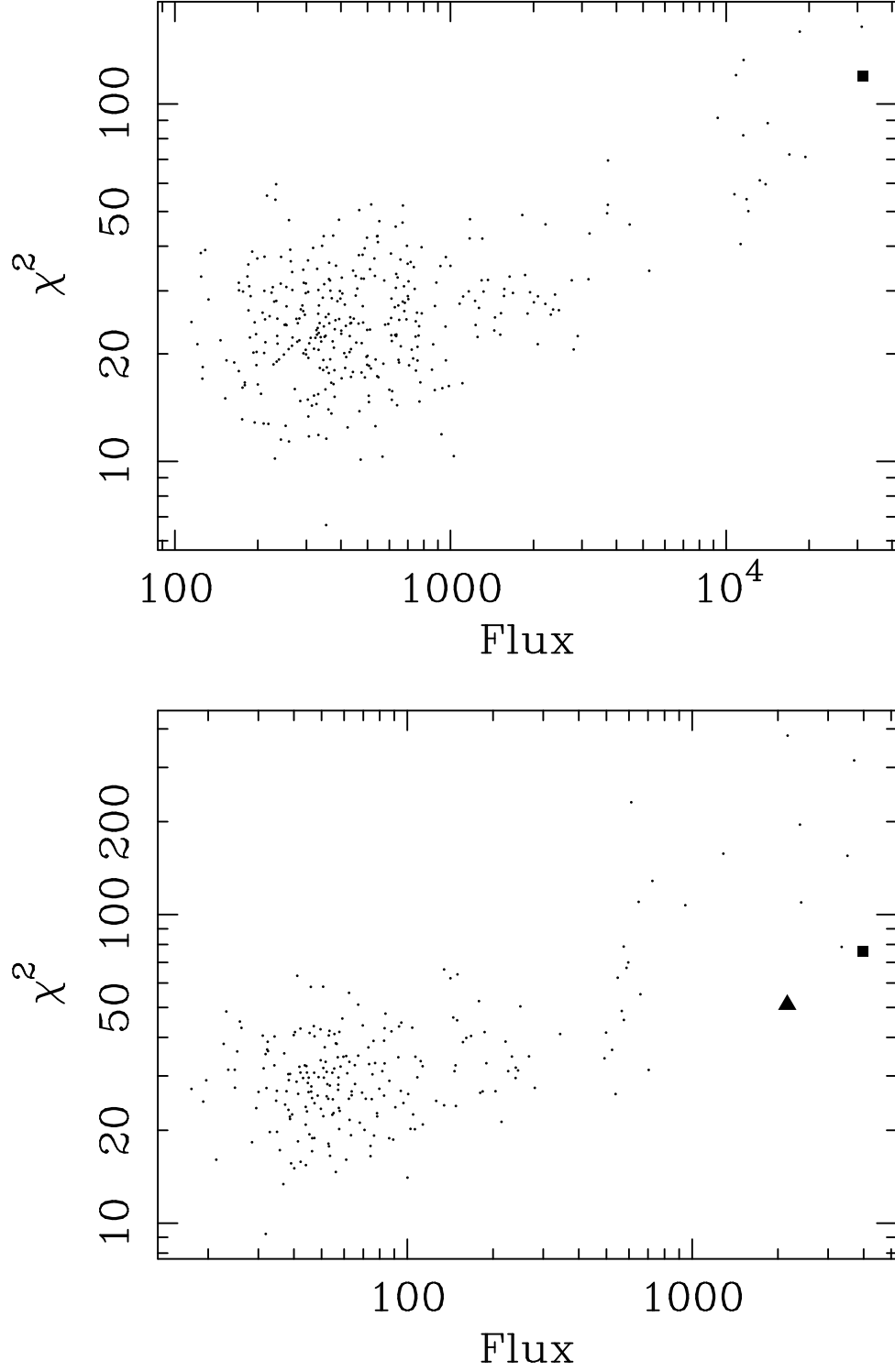


Fig. 9.— a) Plot of  $\chi^2$  *versus* total flux for each object in the fiducial STIS image. The solid square is the QSO. b) The same plot for the fiducial PC image. The solid square and triangle correspond to images A and B, respectively, of the lensed QSO.

–0.058	–0.060	–0.071	–0.026	–0.018
–0.108	–0.119	–0.111	–0.063	–0.050
–0.029	0.017	0.008	0.039	–0.005
–0.126	–0.009	0.003	0.038	–0.079
–0.035	0.007	0.045	0.012	–0.024
–0.131	0.012	0.367	0.006	–0.092
–0.037	0.034	0.028	0.040	–0.034
–0.118	0.019	0.020	0.015	–0.091
–0.046	0.028	0.073	0.022	0.035
–0.115	–0.070	0.015	–0.050	–0.080

Fig. 10.— The mean flux residual as a function of position within the science data array for the fiducial STIS image. The top number in a square tile is the mean over all objects of the fractional difference between the value of the science data pixel and the fitted value. The bottom number is the mean of the difference between the value of the science data pixel and the fitted value divided by the uncertainty in the pixel value.



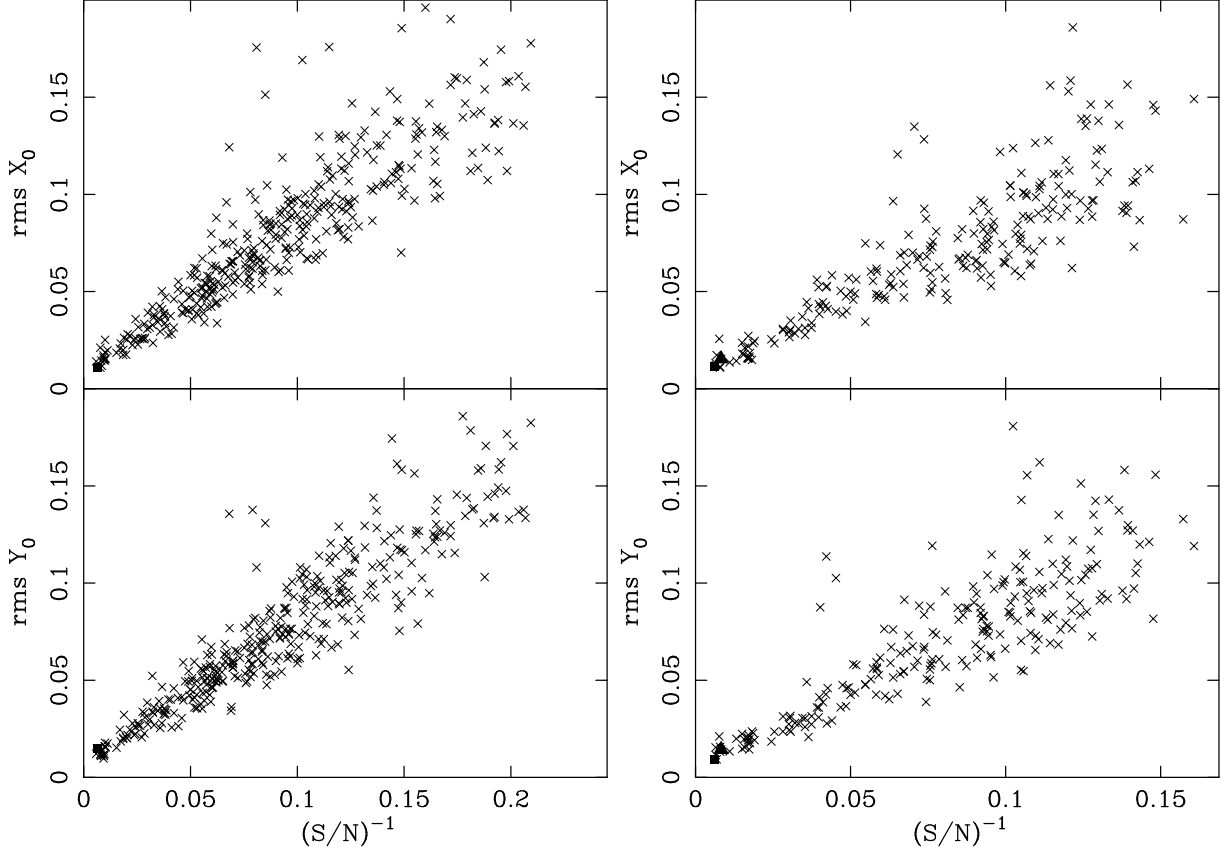


Fig. 11.— a) The *rms* scatter of  $X_0$  (top) and  $Y_0$  (bottom) around their means *versus* the inverse of the  $S/N$  for all objects with at least two measured centroids in the first-epoch images taken with STIS for the FOR J0238–3443 field. The solid square is the QSO. b) The same as (a) for objects in the first-epoch images taken with the PC for the FOR J0240–3434 field. The solid triangle is the second image of the lensed QSO.

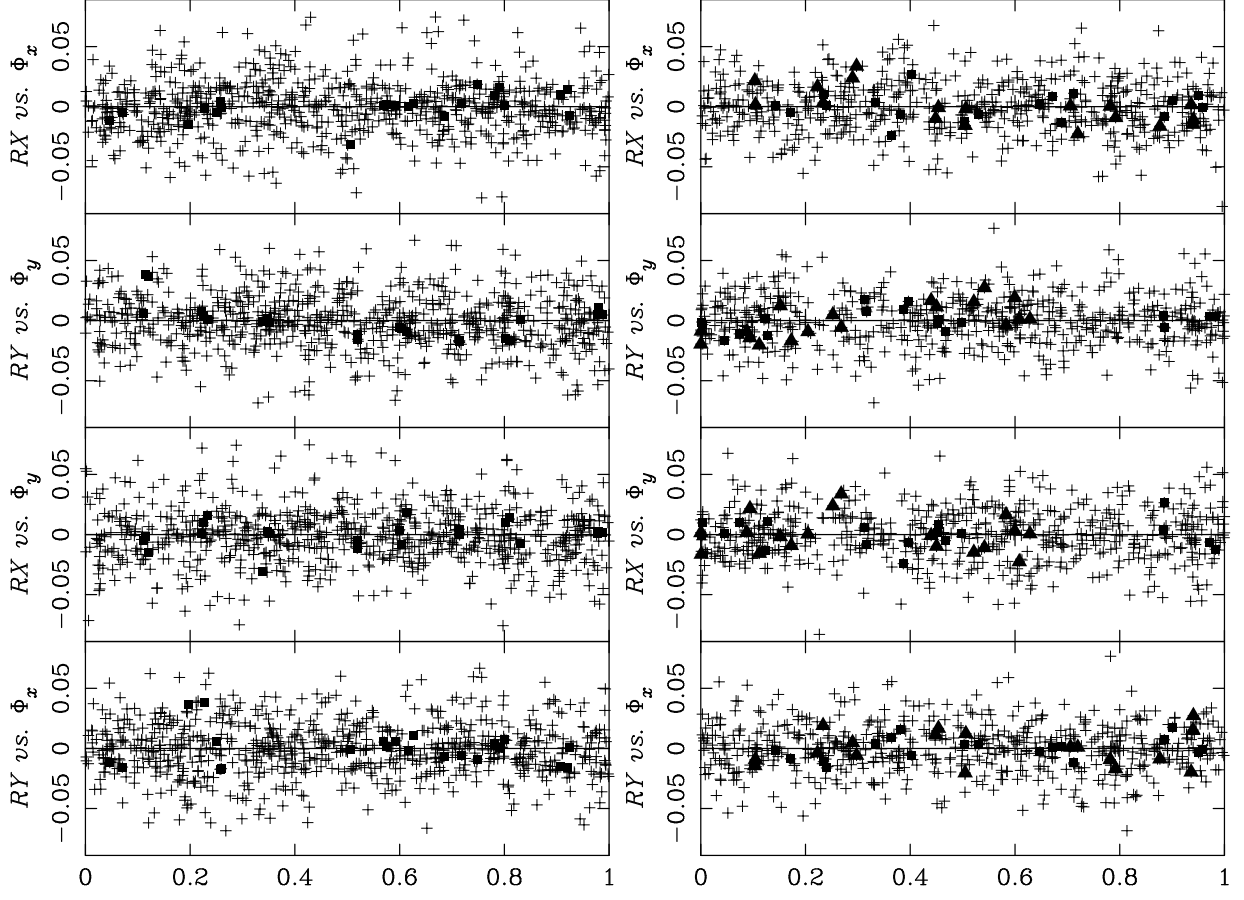


Fig. 12.— a) From top to bottom, the four panels show  $\mathcal{RX}$  versus the pixel phase  $\Phi_x$ ,  $\mathcal{RY}$  versus the pixel phase  $\Phi_y$ ,  $\mathcal{RX}$  versus  $\Phi_y$ , and  $\mathcal{RY}$  versus  $\Phi_x$ . All of the panels show the objects contributing to the construction of the ePSF for the first-epoch images taken with STIS for the FOR J0238 – 3443 field. The solid square is the QSO. b) The same as (a) for objects in the first-epoch images taken with the PC for the FOR J0240 – 3434 field. The solid triangle is the second image of the lensed QSO.

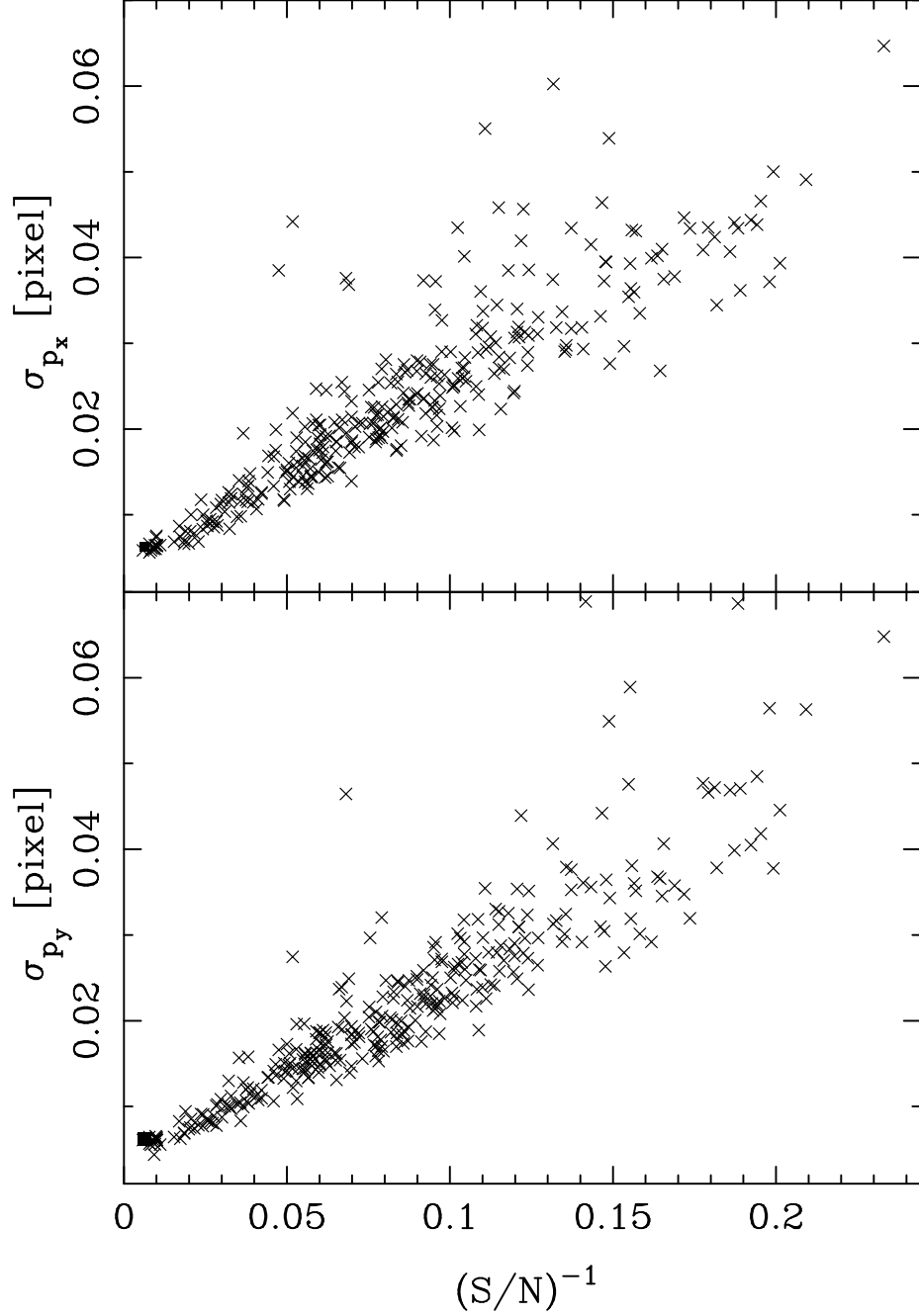


Fig. 13.— The uncertainty in  $p_x$ ,  $\sigma_{p_x}$ , (top) and the uncertainty in  $p_y$ ,  $\sigma_{p_y}$ , (bottom) plotted *versus* the inverse of the average  $S/N$ . The data are from epoch 2000 and 2001 for the FOR J0238 – 3443 field. The  $S/N$  is from the earlier epoch. The solid square is the QSO.

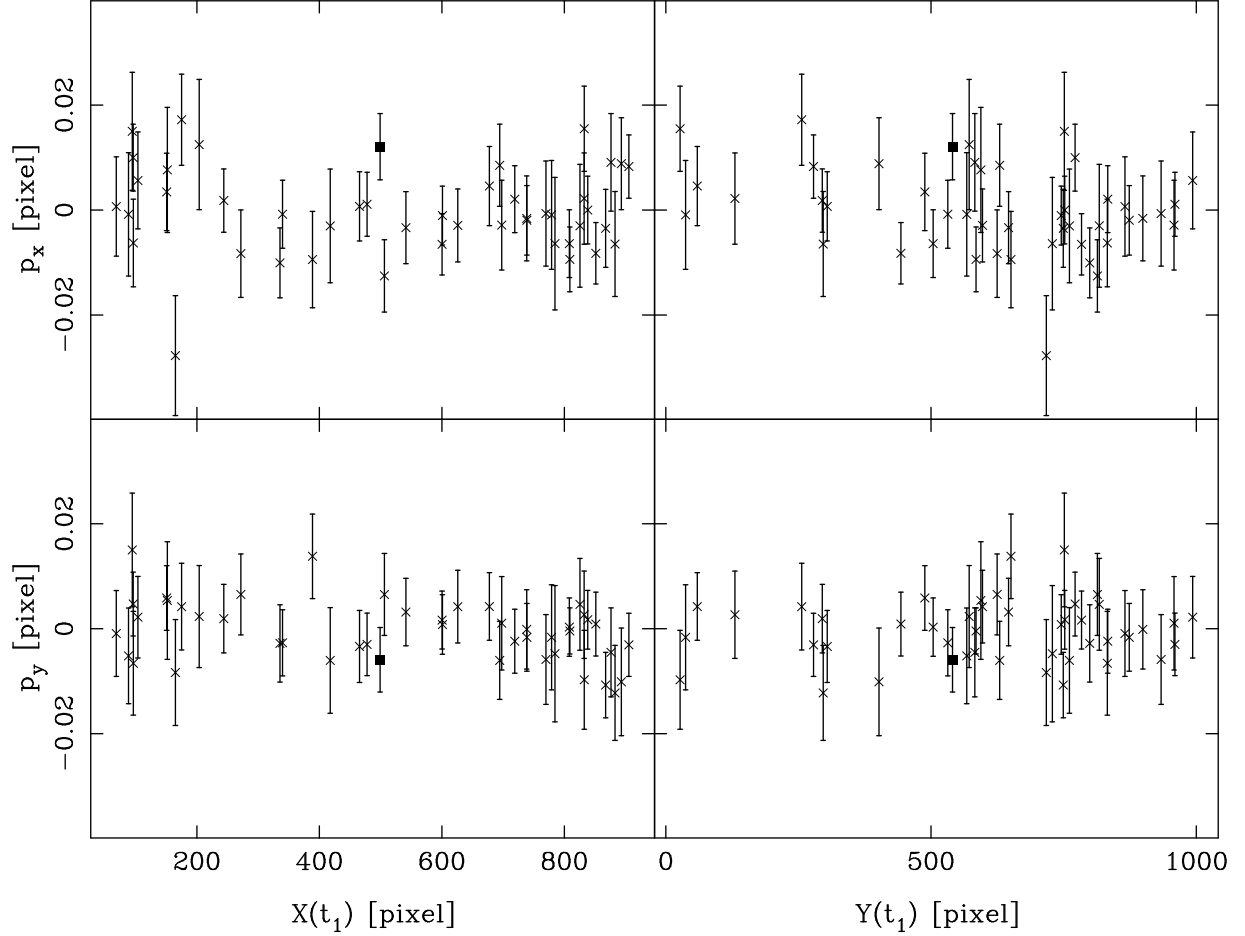


Fig. 14.— The components of the difference in the two centroids of an individual object in the standard coordinate system,  $p_x$  and  $p_y$ , plotted *versus* location in the image for the FOR J0238 – 3443 field. The two centroids for an object are from epoch 2000 and 2001. Only objects with  $S/N > 30$  are shown. The solid square is the QSO. The left-hand panels plot  $p_x$  (top) and  $p_y$  (bottom) *versus*  $X(t_1)$  — the  $X$  coordinate in the epoch 2000 fiducial image — and the right-hand panels similarly plot the same quantities *versus*  $Y(t_1)$  — the  $Y$  coordinate in the epoch 2000 fiducial image.

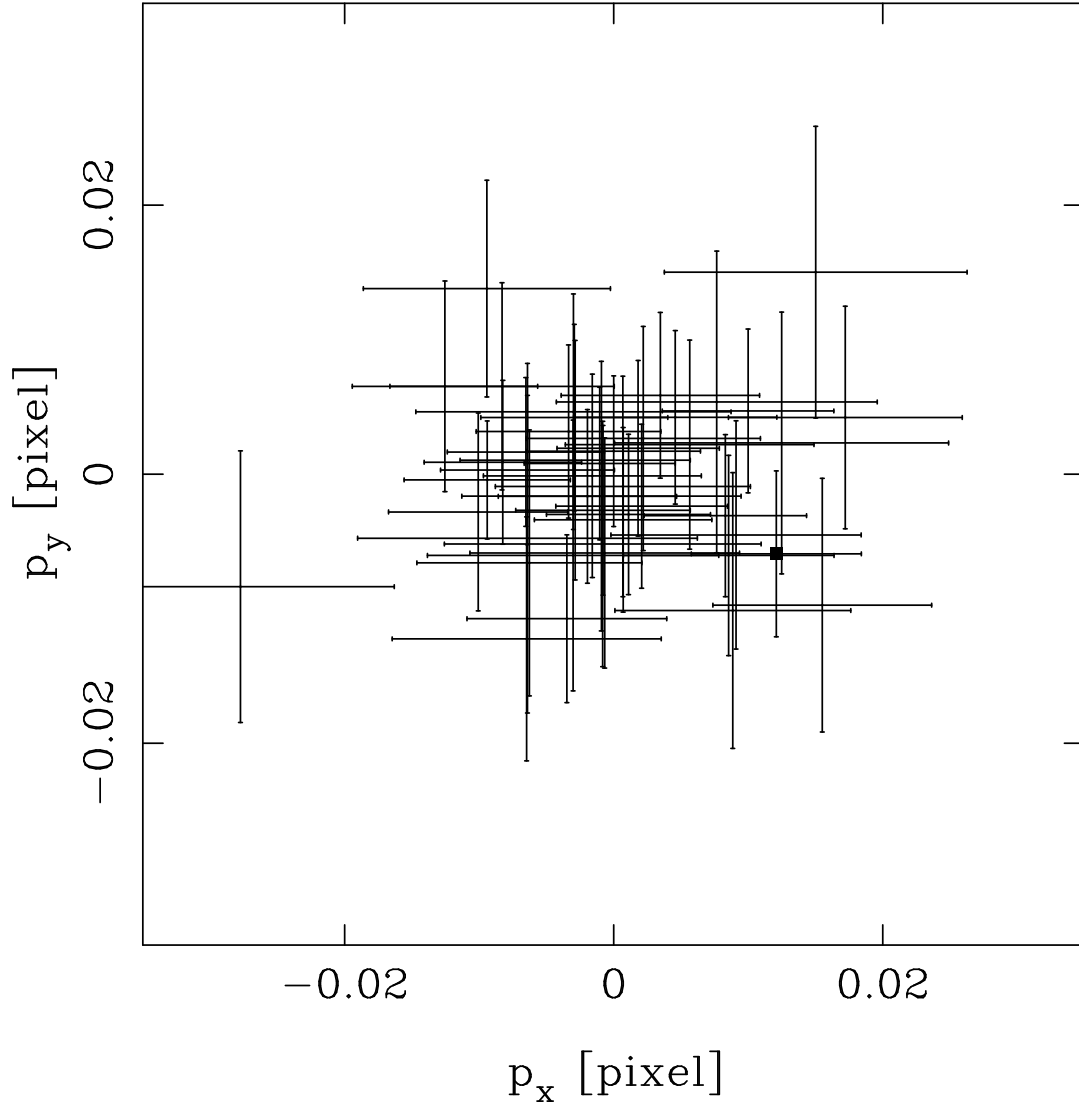


Fig. 15.— Plot of  $p_y$  versus  $p_x$  for the 45 objects with  $S/N > 30$  in the FOR J0238 – 3443 field using epoch 2000 and 2001 data. The solid square is the QSO.

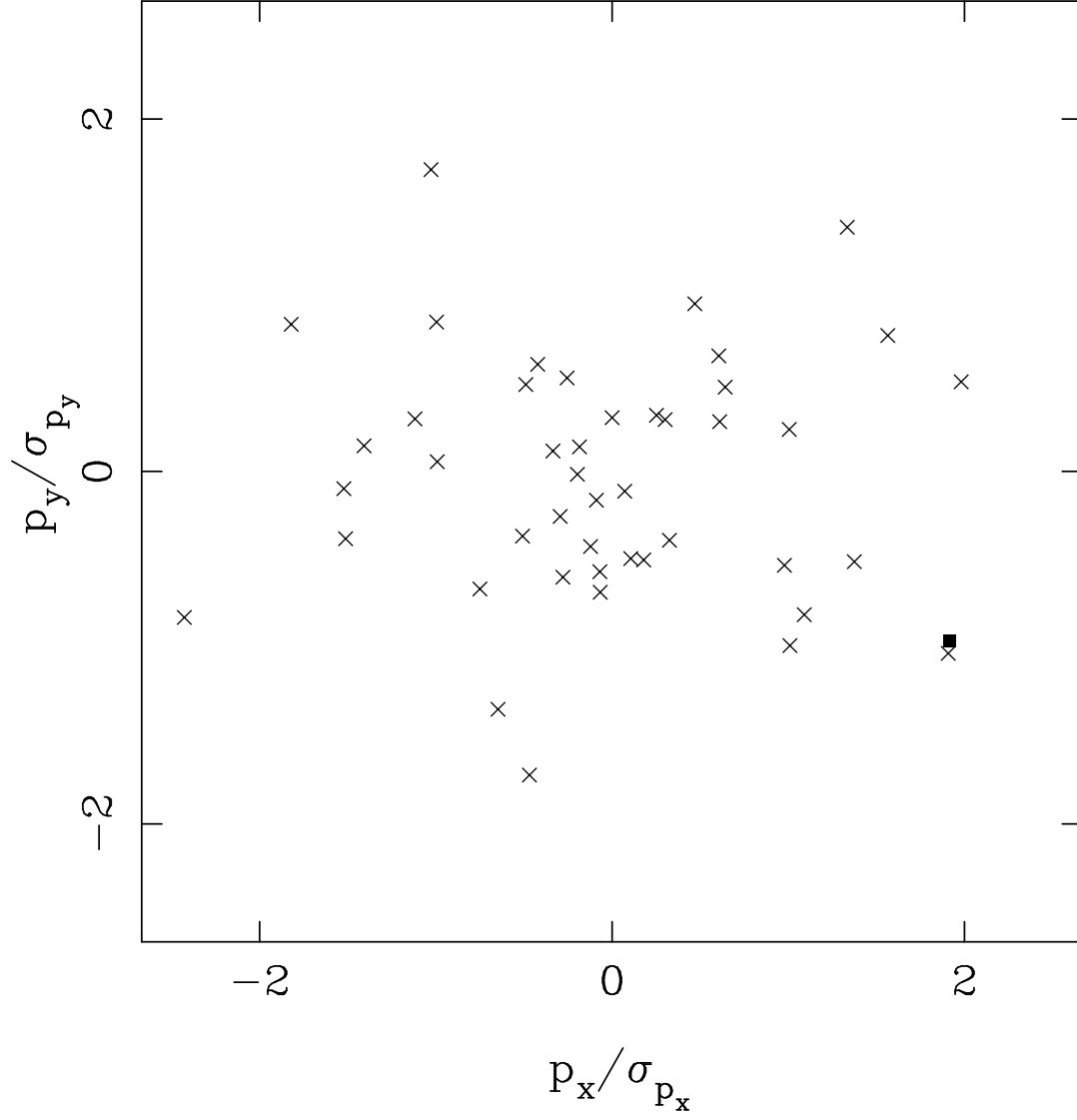


Fig. 16.— Plot of  $p_y/\sigma_{p_y}$  versus  $p_x/\sigma_{p_x}$  for the same objects as in Figure 15.

TABLE 1. Information about Fields and Images

Field (1)	Detector (2)	Date <i>yyyy – mm – dd</i> (3)	$T_{exp}^a$ (s) (4)	R.A. (J2000.0) (5)	Decl. (J2000.0) (6)	$l$ (deg) (7)	$b$ (deg) (8)
CAR J0640 – 5055	STIS	2000 – 04 – 10	$24 \times 207$	06 40 59.20	–50 55 41.00	260.0434	–22.3074
		2001 – 04 – 14	$24 \times 207$				
		2002 – 04 – 06	$24 \times 206$				
CAR J0641 – 5057	PC	1999 – 04 – 17	$18 \times 160$	06 41 51.60	–50 57 12.99	260.1112	–22.1824
		2001 – 04 – 14	$18 \times 160$				
		2002 – 03 – 27	$18 \times 160$				
FOR J0238 – 3443	STIS	2000 – 03 – 08	$24 \times 193$	02 38 43.80	–34 43 53.00	237.8945	–65.8545
		2001 – 03 – 08	$24 \times 192$				
		2003 – 03 – ...	...				
FOR J0240 – 3434	PC	1999 – 03 – 10	$18 \times 160$	02 40 07.70	–34 34 20.01	237.3849	–65.6013
		2001 – 03 – 08	$16 \times 160$				
		2003 – 03 – ...	...				
FOR J0240 – 3438	STIS	2000 – 01 – 31	$24 \times 192$	02 40 38.70	–34 38 58.00	237.5224	–65.4828
		2001 – 01 – 25	$24 \times 192$				
		2002 – 01 – 29	$24 \times 192$				
SCL J0100 – 3341	STIS	2000 – 09 – 24	$24 \times 192$	01 00 25.30	–33 41 07.00	287.0321	–83.1634
		2002 – 09 – ...	...				
SCL J0100 – 3338	STIS	1999 – 09 – 13	$24 \times 193$	01 00 32.60	–33 38 32.00	286.7212	–83.1971
		2000 – 09 – 28	$24 \times 193$				
		2002 – 09 – ...	...				
UMI J1508 + 6717	PC	1999 – 03 – 14	$40 \times 160$	15 08 40.41	67 17 47.49	105.0842	44.7801
		2001 – 03 – 10	$36 \times 160$				
		2003 – 02 – ...	...				
UMI J1508 + 6716	STIS	2000 – 02 – 16	$24 \times 351$	15 08 37.50	67 16 33.50	105.0684	44.7979
		2001 – 02 – 15	$24 \times 352$				
		2002 – 02 – 01	$24 \times 210$				

<sup>a</sup>Number of images times the mean exposure time. The actual exposure times of individual images may differ by a few percent from the mean due to constraints imposed by the orbit of HST.

TABLE 2. Distortion Coefficients

Subscript	STIS		WFPC2	
	$C$	$D$	$C$	$D$
0	0.0	0.0	354.356	343.646
1	1.0011324	$-5.6351965 \times 10^{-5}$	$1000.21 \times 10^{-3}$	$2.64983 \times 10^{-3}$
2	$-1.2427886 \times 10^{-4}$	1.0006398	$1.68510 \times 10^{-3}$	$999.790 \times 10^{-3}$
3	$-3.9052366 \times 10^{-7}$	$1.4414957 \times 10^{-7}$	$-0.476421 \times 10^{-6}$	$-0.915545 \times 10^{-6}$
4	$-2.3388352 \times 10^{-7}$	$2.1911561 \times 10^{-6}$	$-0.128977 \times 10^{-6}$	$-0.347576 \times 10^{-6}$
5	$-2.7747067 \times 10^{-6}$	$-1.5699432 \times 10^{-7}$	$-1.11946 \times 10^{-6}$	$0.532097 \times 10^{-6}$
6	$-5.8339901 \times 10^{-9}$	$2.2058683 \times 10^{-10}$	$-38.9898 \times 10^{-9}$	$-2.59264 \times 10^{-9}$
7	$1.4677396 \times 10^{-9}$	$-3.0218644 \times 10^{-9}$	$0.495226 \times 10^{-9}$	$-34.9678 \times 10^{-9}$
8	$-3.4363894 \times 10^{-9}$	$8.2253175 \times 10^{-10}$	$-36.2773 \times 10^{-9}$	$-1.57071 \times 10^{-9}$
9	$6.8542388 \times 10^{-10}$	$-3.1486902 \times 10^{-9}$	$-0.075298 \times 10^{-9}$	$-41.9018 \times 10^{-9}$



TABLE 3. Measured Proper Motion of Fornax

Field (1)	Baseline yyyy $\rightarrow$ yyyy (2)	$\mu_\alpha$ (mas cent $^{-1}$ ) (3)	$\mu_\delta$ (4)
FOR J0238 – 3443	2000 $\rightarrow$ 2001	$50 \pm 31$	$-47 \pm 32$
FOR J0240 – 3434 <sup>a</sup>	1999 $\rightarrow$ 2001	$71 \pm 32$	$-43 \pm 32$
FOR J0240 – 3434 <sup>b</sup>	1999 $\rightarrow$ 2001	$27 \pm 32$	$-60 \pm 32$
FOR J0240 – 3438	2000 $\rightarrow$ 2001	$22 \pm 35$	$-82 \pm 34$
	2001 $\rightarrow$ 2002	$67 \pm 35$	$-49 \pm 35$
	2000 $\rightarrow$ 2002	$49 \pm 18$	$-68 \pm 18$
Weighted Average and Uncertainty <sup>c</sup>		$49 \pm 13$	$-59 \pm 13$

<sup>a</sup>With respect to image A of the QSO (Tinney 1995).

<sup>b</sup>With respect to image B of the QSO (Tinney 1995).

<sup>c</sup>The calculation uses the value for only the 2000 $\rightarrow$ 2002 time baseline for FOR J0240 – 3438, both values for FOR J0240 – 3434, and the one value for FOR J0238 – 3443.

TABLE 4. Galactic-Rest-Frame Proper Motion and Space Velocity of Fornax

Field (1)	Baseline yyyy → yyyy (2)	$\mu_{\alpha}^{\text{Grf}}$ (mas cent <sup>-1</sup> ) (3)	$\mu_{\delta}^{\text{Grf}}$ (mas cent <sup>-1</sup> ) (4)	$\mu_l^{\text{Grf}}$ (mas cent <sup>-1</sup> ) (5)	$\mu_b^{\text{Grf}}$ (mas cent <sup>-1</sup> ) (6)	$\Pi$ (km s <sup>-1</sup> ) (7)	$\Theta$ (km s <sup>-1</sup> ) (8)	$Z$ (km s <sup>-1</sup> ) (9)	$V_r$ (km s <sup>-1</sup> ) (10)	$V_t$ (km s <sup>-1</sup> ) (11)
FOR J0238 – 3443	2000→2001	26 ± 31	–25 ± 32	20 ± 32	31 ± 31	150 ± 200	–150 ± 200	110 ± 80	–30 ± 120	240 ± 190
FOR J0240 – 3434 <sup>a</sup>	1999→2001	48 ± 32	–21 ± 32	12 ± 32	51 ± 32	280 ± 200	–110 ± 200	170 ± 90	–30 ± 120	340 ± 190
FOR J0240 – 3434 <sup>b</sup>	1999→2001	4 ± 32	–38 ± 32	37 ± 32	11 ± 32	20 ± 200	–240 ± 200	60 ± 90	–40 ± 120	250 ± 200
FOR J0240 – 3438	2000→2001	–1 ± 35	–60 ± 34	59 ± 34	10 ± 35	0 ± 220	–390 ± 220	60 ± 90	–50 ± 130	390 ± 220
	2001→2002	44 ± 35	–28 ± 35	19 ± 35	48 ± 35	260 ± 220	–160 ± 220	160 ± 90	–30 ± 130	340 ± 200
	2000→2002	26 ± 18	–47 ± 18	41 ± 18	34 ± 18	160 ± 110	–290 ± 110	120 ± 50	–40 ± 60	350 ± 110
Weighted Average and Uncertainty <sup>c</sup>		26 ± 13	–38 ± 13	32 ± 13	33 ± 13	160 ± 80	–230 ± 80	120 ± 40	–40 ± 50	310 ± 80

<sup>a</sup>With respect to image A of the QSO (Tinney 1995).

<sup>b</sup>With respect to image B of the QSO (Tinney 1995).

<sup>c</sup>The calculation uses the value for only the 2000→2002 time baseline for FOR J0240 – 3438, both values for FOR J0240 – 3434, and the one value for FOR J0238 – 3443.